Test and performance of novel Super Fine-Grain scintillation Detectors as active target for future neutrino experiments

Federico Nardi

Thesis submitted for the degree of
Master in Nuclear and Particle Physics

Department of Physics
Faculty of mathematics and natural sciences

UNIVERSITY OF OSLO

Autumn 2020

Test and performance of novel Super Fine-Grain scintillation Detectors as active target for future neutrino experiments

Federico Nardi

Abstract

We present a study of performance and energy resolution of a novel Super Fine-Grained Detector (SFGD) prototype. Data were collected during the second test run at the CERN T9 beam line and include pion, proton, muon and electron events for different magnetic field configurations (0T, 0.2T and 0.7T). The design consists in an array of $1cm$ side scintillator cubes with wavelength shifting readout fibers and has been developed for the upgrade of the Tokai-to-Kamiokande (T2K) Near Detector ND280. The upgrade is inserted in the context of aiming towards higher precision measurements of neutrino oscillations to determine neutrino masses and the leptonic CP violation phase, which will shed light in the matter-antimatter asymmetry measured in the Universe today. This novel detector design will find large use in the coming generation of neutrino experiments for its versatile geometry and the good tracking and energy resolution. We find that the average light yield per MIP (Minimum Ionizing Particle) is 52.6 ± 6.4 photoelectrons, compatible with tests on different prototype geometry, and improving the ND280 Energy Resolution from $\sim 20\%$ to $\sim 11\%$. We run a tentative search for magnetic bending effect reported elsewhere, without being able to measure a net effect due to scarce statistics. We also present an overview of the state of the art measurements and theoretical models in neutrino physics, and discuss further developements towards precision leptonic CP measurements, with particular focus on the proposal for a Neutrino Super Beam experiment at the European Spallation Source facility (ESSνSB).

Acknowledgements

First and foremost I would like to thank my main supervisor Farid Ould-Saada for introducing me to the field of Particle Physics. Your enthusiasm and invaluable insights have allowed me to understand more and more about physics and my project. A special thanks also to my co-supervisor Eirik Gramstad, for the great help provided throughout this work and for being open to useful discussions at any time.

A worker is only as good as his officemates at times, and I am no exception. A big thanks to my office-mates and corridor-mates in the High Energy Physics (HEP) group at University of Oslo for the great support and social environment. And coffee.

I would be remiss if I did give a big, special thank you to Mona. Not just for being my desk neighbour in the office, but for effectively going through this process with me: for sharing the highs and lows, the frustrations; for being around for the the long days (and nights), for getting pizza and McDonald's; for helping me whenever I needed. It's no understatement to say I couldn't have done this without you.

Another big thank you goes to Jake, for keeping up the motivation and always being around for discussions, listening to my complaints, and for trolley problem talks -and for proofreading and spell checking the whole thesis.

On the less academic (but no less important) side of things, this year has - naturally - been a very bizarre one with COVID, and more specifically, being in lockdown for several months. I'd like to give a big thanks to Ayaka and Einar, my flatmates, who kept me sane and motivated during the dark times.

Finally, it's needless to mention that this work would not have been possible without the support of my parents, on whose unconditional support I could always rely.

Contents

Chapter 1

Introduction and motivation

This study considers the analysis in terms of performance and energy resolution of the data from a Super Fine-Grained Detector prototype during the test run held in August-September 2018 at the European Research Center CERN. The detector considered is an array of 1cm^3 side cubes of a newly developed crystal scintillator, whose design has been studied for the proposed upgrade of the near detector for the Tokai-to-Kamiokande (T2K) long-baseline experiment [3]. This design concept is also included in the conceptual design of the near detector for the Neutrino Super Beam at the European Spallation Source (ESSνSB) in Lund, which partakes in a new generation of neutrino experiments aiming at precision measurements of leptonic CP violation, the violation of the fundamental symmetry between particles and antiparticles, and neutrino masses. In order to reach the desired precision, efforts will be concentrated in constructing higher-intensity beams, improving the efficiency and performances of detection techniques and reducing to the minimum systematic uncertainties and background noise. In this chapter we introduce the state of the art of the current neutrino physics experiments and describe the goals of the ESSνSB concept, that serves as a context for the SuperFGD test measurements, also in relation to the two main "competitors", Tokai-to-Hyper-Kamiokande (T2HK) in Japan, and the Deep Underground Neutrino Experiment (DUNE) in the United States.

1.1   Neutrino measurements

The first important results of neutrino measurements that started to focus more interest in the field were the ones on atmospheric and solar neutrino fluxes, respectively the neutrino events registered from cosmic rays and decay processes in the Earth atmosphere and the neutrino events coming from fusion processes in the Sun. Those measurements in fact show a significant deviation from the expected neutrino flavour fluxes from the Sun, and the disappearance of neutrino

flavours between the interaction point in the atmosphere and the detector.

1.1.1 Atmospheric neutrinos

Atmospheric neutrinos are the results of the interactions of cosmic rays with the Earth's atmosphere, leading to the appearance of hadrons. A fraction of those are pions that subsequently decay through

$$\pi^+ \to \mu^+ + \nu_\mu$$
$$\pi^- \to \mu^- + \bar{\nu}_\mu$$

followed by

$$\mu^- \to \nu_\mu + e^- + \bar{\nu}_e$$
$$\mu^+ \to \bar{\nu}_\mu + e^+ + \nu_e.$$

This implies that it is possible to measure the flux of electron and muon neutrinos on Earth and compare it with the expectations to reveal potential neutrino flavour oscillations. The 1998 results from Super Kamiokande [33] come from a water Cherenkov detector built 6km underground, to remove all the possible signals except for muons and neutrinos. The goal is to observe a deviation from the expected muon flux compatible with the oscillation of muon neutrinos into tau neutrinos, with a strong dependence on the zenith angle, to prove that it depends on the distance travelled by the neutrino from the production point to the detector. Figure 1.1 shows the results obtained by Super Kamiokande on the neutrino appearances as function of zenith angle, compared with both no oscillation and muon to tau oscillation models. The data is clearly compatible with oscillating neutrino states that cause disappearance of neutrino species with respect to the non-oscillating prediction.

1.1.2 Solar neutrinos

Solar neutrinos are the ones produced in nuclear processes in the Sun. The main contribution comes from the fusion process $p+p \to D+e^+ +\nu_e$. However, because of the low deuteron (D) binding energy ($\sim 2.2\text{MeV}$), the low-energy neutrinos produced ($< 0.5\text{MeV}$) are hard to detect. Thus the experiments are more sensitive to neutrinos produced for instance by the β-decay of ^8B produced from helium fusion

$$^8_5B \to^8_4 Be^* + e^+ + \nu_e$$
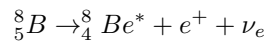
with energies up to 15MeV.

Both Super-Kamiokande and SNO experiments, using Cherenkov detection for solar neutrinos, registered a flux from the Sun that is lower than the predicted
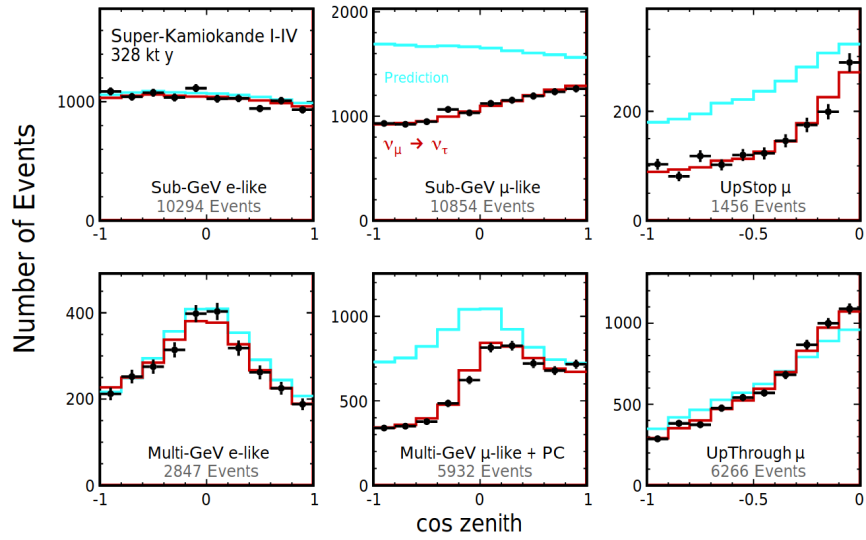
Figure 1.1: Atmospheric neutrino detections as a function of different zenith angles for different event selections. From [32] via [63].
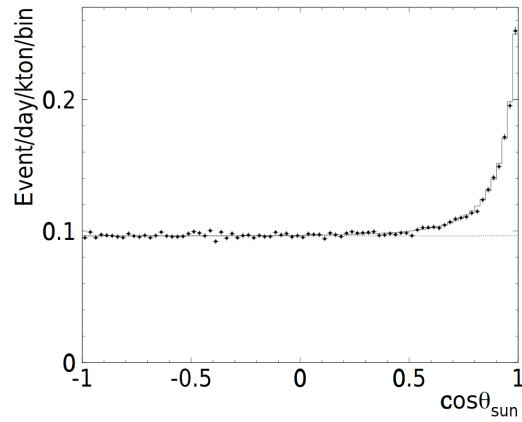

Figure 1.2: Super-Kamiokande solar neutrino data as function of polar angle with the Sun. From [31].

value form the sole interaction rates, thus providing evidence for oscillations of the electron neutrino flavour. Note that SNO uses heavy water $D_2 0$ instead of H_2O and the lower binding energy of deuteron allows for the detection of multiple neutrino interactions with different sensitivities [64]. Figure 1.2 for instance shows the distribution of solar neutrino events from Super Kamiokande as function of the polar angle with the Sun. The dashed line corresponds to the estimated background from radioactive isotope decays.

Those experiments lead to the discovery of Neutrino oscillations, the oscillations in flavour of a free propagating neutrino state that resulted in the 2015 Nobel Prize in Physics [58]. This proved that the originally assumed massless neutrinos actually have a mass, even if it is very small ($\leq$ 1eV). It is however only an initial achievement in the research on neutrino physics. Many questions are still not answered and the efforts of the research community are concentrated to answer three fundamental questions:

- What are the values of neutrino masses and what is their ordering?

- Is CP symmetry violated in neutrino interactions?

- Are neutrino Dirac or Majorana particles?

An exhaustive overview of these topics is presented in Chapter 2.

1.1.3 Neutrino Oscillations and beyond: precision measurements

Neutrino oscillations are explained in terms of the mixing between mass eigenstates ν_1, ν_2, ν_3 (free particle states) and flavour eigenstates ν_e, ν_μ, ν_τ (states produced in a weak interaction). This process is controlled by three mixing angles $\theta_{13}, \theta_{23}, \theta_{12}$, a complex phase δ responsible for CP violation and the difference between the squared neutrino masses Δm_{12}^2, Δm_{13}^2 and Δm_{23}^2. Solar and atmospheric results introduced above are therefore interesting because they are each sensitive to one of the two neutrino mass splittings, respectively Δm_{32}^2, also known as atmospheric mass splitting Δm_{atm}^2, and Δm_{12}^2, also known as solar mass splitting Δ_{sol}^2. Note that only two of the three mass differences are independent and the third can be expressed in terms of the other two. We will describe with enough details the process in Chapter 2, but now let us just focus on those parameters, whose experimental values are listed in table 1.1

First of all, we should note that when we are considering the values Δm^2 we can define two possible orderings: one where the heaviest state is ν_3 and the lightest is ν_1, and one where the heaviest is ν_2 and the lightest is ν_3. The former is known as *normal ordering*, while the latter is known as *inverted ordering*. The determination of which of the two orderings is verified in Nature is known as the *neutrino hierarchy problem*. Figure 1.3 sketches the two different possible orderings (not in scale).

Secondly, we can see that if we measure and characterize with enough precision the behaviour of neutrino oscillations, we can not only try to attack the

parameter	inverted	normal
$\sin^2(\theta_{12})$	0.307 ± 0.013	
$\sin^2(\theta_{23})$	$0.421^{+0.033}_{-0.025}$	$0.0417^{+0.025}_{-0.028}$
$\sin^2(\theta_{13})$	$(2.12 \pm 0.08) \times 10^{-2}$	
Δm^2_{21}	$(7.53 \pm 0.18) \times 10^{-5} \text{eV}^2$	
Δm^2_{32}	$(-2.56 \pm 0.04) \times 10^{-3} \text{eV}^2$	$(2.51 \pm 0.05) \times 10^{-3} \text{eV}$
δ_{CP} (3σ)	[-2.54,-0.32]rad	[-3.41,-0,03]rad

Table 1.1: Neutrino oscillations parameters for inverted and normal mass hierarchy. Results taken from the PDG Reviews [63] except for δ_{CP}, coming from [23].
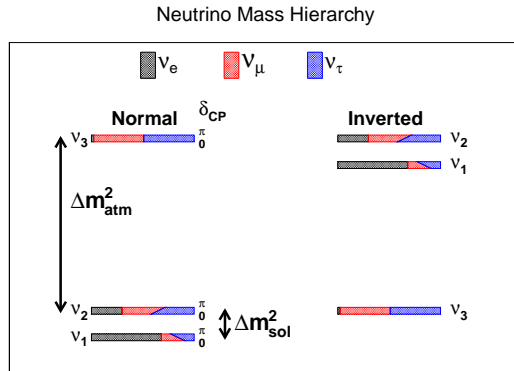

Figure 1.3: Illustration of the neutrino mass hierarchy problem

hierarchy problem, but also have a measurement for the CP violating phase δ. A first constraint for this value has been provided only recently (April 2020) and it is still not clear whether or not we can measure non-zero CP violation also in the lepton sector of the Standard Model. This is crucial as it can give new insights in the symmetries of particle physics. It is also directly connected to cosmology and the history of the Universe, since it is one of the key elements to explain baryogenesis and leptogenesis, linked by possible Beyond the Standard Model unifying theories, and the fact that matter seems to be dominant in the universe as no antimatter counterpart is measured.

In this context, the need for highly precise measurements of neutrino oscillations phenomena emerges as an important research direction to tackle very fundamental questions within multiple branches of Physics, from Particle Physics to Cosmology, including Astrophysics and Nuclear Physics. A new generation of long-baseline experiments is currently being planned with the objective of constraining and providing a measurement of δ_{CP} and determining the neutrino masses. Very promising results are expected to come within the next decades. There are three main experiments which has been proposed:

- Deep Underground Neutrino Experiment (DUNE) [22], a long-baseline experiment at Fermilab, in the United States;

- Tokai to Hyper-Kamiokande (T2HK), essentially the upgrade of the current T2K facilities [16];

- The Neutrino Super Beam at the European Spallation Source (ESSνSB)[55], inserted in the broader context of creating a new leading facility in neutrino experiments in Europe.

While the first two experiments are expected to start data acquisition in 2027, the time scale for ESSνSB is a bit longer, as it is still in the conceptual design phase.

1.2 Long-baseline neutrino experiments

The advancements in particle accelerator technology have enabled us to generate high-energy neutrino beams that can be studied to make precision measurements on the oscillations and CP parameters. Those beams can be produced by sending a proton beam into a target, thus producing a multitude of hadrons. Most of those hadrons are charged pions $\pi^{\pm}$, that can be selected and focused within a region (typically with length of a few hundred meters $\sim \beta c \tau_{\pi}$) where they can decay via the process

$$\pi^+ \to \mu^+ + \nu_{\mu}$$
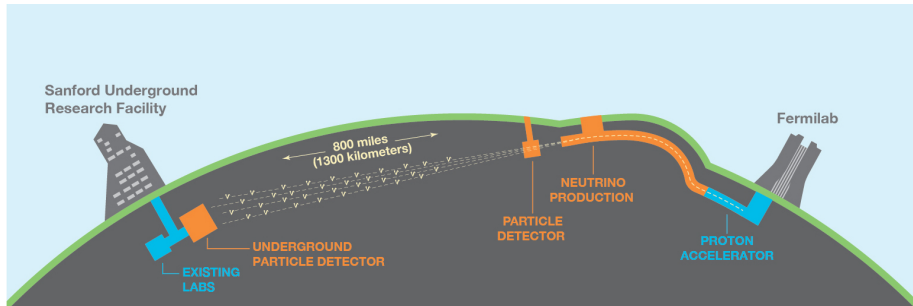$$\pi^- \to \mu^- + \bar{\nu}_{\mu}.$$

Figure 1.4: Sketch of the DUNE [22] baseline design.

Successively, in a typical long-baseline experiment the measurements are taken by comparing data from two detectors: a Near Detector (ND) right after the decay tunnel, and a Far Detector (usually a Cherenkov tank) (FD). In this way it is possible to compare the unoscillated neutrino spectra from the ND with the oscillated spectra from the FD. Figure 1.4 shows a sketch of the Deep Underground Neutrino Experiment (DUNE) in the US. The Neutrino beam is produced at the Fermilab site, where the Near Detector is situated, and then it meets the far detector at Sanford Underground Research Facility after propagating for 1300 kilometers.

One of the main advantage of those kind of experiments is that they can be tailored to take a specific measurement, by determining the length-to-energy ratio L/E that controls the neutrino flavour oscillation. It is therefore possible to select the energy of the neutrino beam such that for instance the first oscillation peak coincides with the site of the far detector. This is indeed the case of the DUNE [22] and Tokai-to-Kamiokande (T2K) [3] experiments, aiming to perform precision CP measurements from oscillations data.

1.3 Towards leptonic CP violation

The relatively recent measurement of $\theta_{13} \sim 8°$[63], initially expected to be much smaller, opened new insights in terms of the possible measurements on both CP violation and neutrino mass hierarchy. In fact, for a large θ_{13} it is possible to show that just measuring the oscillation probabilities at the second oscillation maximum instead of the first one would increase the sensitivity for δ_{CP} by about a factor 3 [24]. Figure 1.5 shows the neutrino oscillation probability as a function of the length-to-energy ratio that determines the oscillation scale. At the first peak the atmospheric contribution is dominant, whereas in correspondence with the second one the CP maximum is of the same order as the atmospheric contribution (the solar term provides a minor contribution in bot cases and is at all effects negligible). This hints that a detection at L/E corresponding to the second peak would have a better sensitivity to the matter-antimatter
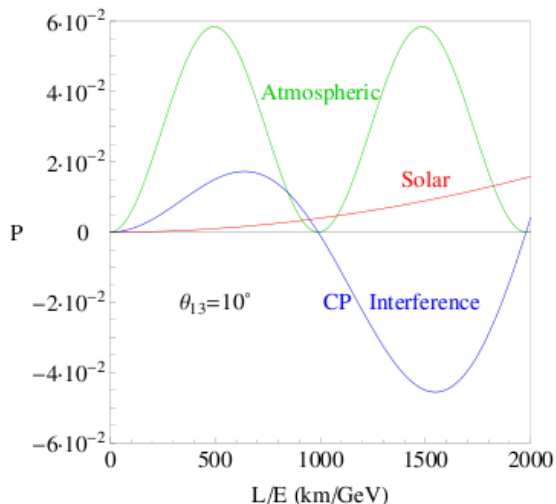
Figure 1.5: Oscillation probability for solar neutrino, atmospheric neutrinos and the CP interference term as a function of the scale parameter L/E. From [24]

asymmetry.

This would basically imply that the parameter could be determined well beyond the 5σ confidence needed, and thus provide a strong constraint on leptonic CP violation, as well as further constraints on the mass hierarchy problem and the origins of CP violation itself.

1.3.1 EuroNuNet and ESSνSB

In this direction has been moving the work of the EuroNuNet project [56], a networking initiative whose main aim is to aggregate a European community for neutrino studies and push towards the development of a new concept of neutrino oscillation experiment. The collaboration, comprising 13 countries, and operating from 2016 to 2020, had the purpose of demonstrating the possibility of producing the world's most intense neutrino beam from the proton linear accelerator (LINAC) being constructed at the European Spallation Source (ESS) in Lund, as well as the possibility to build a large underground Far Detector at a 500km distance from the near target. In order to do so, the ESS neutrino Super Beam (ESSνSB) [55] Study Design project was initiated, with the goal to present a conceptual Design Report to organize the European physicists and accelerator engineers communities, together with the ESS site and the Garpenberg Mining Company, responsible for the planned site of the FD. If all the plans are approved, the experiment should start collecting data in 2037.

Baseline design   The concept for the near detector of ESSνSB consists in two devices: an upstream Cherenkov detector, which provides flux monitoring information and event rate measurements, and an active target made of an array of $1 \times 1 \times 1\text{cm}^3$ scintillation cubes with Wavelength-shifting fibers used for readout. Those cubes, whose response study is the object of this thesis, are produced according to the Super Fine-Grained Detector (SuperFGD) design developed for the upgrade of T2K [16]. The advantage of using such a system for the near detector is that it provides an isotropic geometry ideal for identifying low-energy neutrino interactions, where the scattering angles are larger.

The far detector is supposed to follow the MEMPHYS Far Detector design [12] and can be located in two existing mining sites: Zingkuvran, about 360km from the ESS site, and Garpenberg, at $\sim$ 540km from ESS. Since the detector design consists of two modules, the proposal is also considering placing one for each site [37].

Chapter 2

Theoretical overview

The purpose of this chapter is to present a theoretical overview of the methods used in particle physics and the Standard Model. We will in particular focus on the idea of symmetries, as they relate to CP violation, the combined violation of Charge conjugation and Parity symmetries. Since the measurement of CP violation in the lepton sector requires a good understanding of both components of the leptonic isospin doublets, i.e. also neutrinos, a brief overview of neutrino physics is presented. For the first part of this chapter we will mainly follow the theoretical framework as illustrated in Peskin and Schroeder [52], integrating it sometimes with some further insights from Zee [69]. Successively, the main reference will be Thomson's *Modern Particle Physics* [64], integrated with references from the literature, especially when we mention recent results.

2.1 Elements of Quantum Field Theory

The necessity of introducing a field picture instead of a point-like particle arises when trying to include Special Relativity in a Quantum Mechanical framework. Einstein's mass-energy relation and Heisenberg's uncertainty principle combined allow for the creation of particles, and thus considering a fixed number of particles in our theory is inconsistent. We will introduce here the basic ideas of Quantum Field Theory, useful to present the Standard Model of particle physics and to describe quantum fields in a fully relativistic framework.

2.1.1 Classical field theory

Let us consider the fundamental object describing a dynamical system, the Lagrangian L. Since we are now interested in local fields $\phi(x)$ it is useful to define it in terms of the Lagrangian density $\mathscr{L}$, that is a functional acting on the fields themselves and their first derivatives

$$L := \int d^3 x \, \mathscr{L}(\phi, \partial_\mu \phi).$$

The time evolution of the system between two extremes t_1 and t_2 will be such that the action

$$S := \int_{t_1}^{t_2} dt\, L = \int d^4x\, \mathscr{L}$$

is stationary, i.e. a minimum (or maximum). This requirement then translates into

$$0 \overset{!}{=} \delta S$$
$$= \int d^4x \left\{ \frac{\partial \mathscr{L}}{\partial \phi} \delta\phi + \frac{\partial \mathscr{L}}{\partial(\partial_\mu \phi)} \delta(\partial_\mu \phi) \right\}$$
$$= \int d^4x \left\{ \frac{\partial \mathscr{L}}{\partial \phi} \delta\phi + \partial_\mu \left(\frac{\partial \mathscr{L}}{\partial(\partial_\mu \phi)} \delta\phi \right) - \delta\phi\, \partial_\mu \frac{\partial \mathscr{L}}{\partial(\partial_\mu \phi)} \right\}$$
$$= \int d^4x \left\{ \frac{\partial \mathscr{L}}{\partial \phi} - \partial_\mu \frac{\partial \mathscr{L}}{\partial(\partial_\mu \phi)} \right\} \delta\phi$$

where, after a partial integration, we have eliminated the divergence term as we integrate over a domain whose boundary has $\delta\phi = 0$ (initial and final configurations are given). Our integral must vanish for any arbitrary variation $\delta\phi$, thus leading us to the Euler-Lagrange equations, i.e. the equations of motion, for a field:

$$\partial_\mu \frac{\partial \mathscr{L}}{\partial(\partial_\mu \phi)} - \frac{\partial \mathscr{L}}{\partial \phi} = 0. \tag{2.1}$$

One of the most interesting features of the theory is probably the connection between symmetries and conservation laws, as pointed out by Noether's theorem [52]. Let us then consider an infinitesimal transformation

$$\phi(x) \to \phi'(x) = \phi(x) + \alpha \delta\phi(x)$$

and introduce the concept of symmetry:

Def 2.1.1. A transformation $\phi(x) \to \phi'(x)$ is a *symmetry* if the equations of motion are unchanged under its action. Equivalently, a transformation is a symmetry if the Lagrangian $\mathscr{L}$ is invariant under its action, up to a total divergence:

$$\mathscr{L}(x) \to \mathscr{L}(x) + \partial_\mu \mathscr{J}^\mu \qquad \text{for some } \mathscr{J}^\mu$$

Let us try now to vary the Lagrangian $\mathscr{L}$:

$$\delta\mathscr{L} = \frac{\partial \mathscr{L}}{\partial \phi} \delta\phi + \frac{\partial \mathscr{L}}{\partial(\partial_\mu \phi)} \delta(\partial_\mu \phi)$$
$$= \partial_\mu \left(\frac{\partial \mathscr{L}}{\partial(\partial_\mu \phi)} \delta\phi \right) - \left\{ \partial_\mu \frac{\partial \mathscr{L}}{\partial(\partial_\mu \phi)} - \frac{\partial \mathscr{L}}{\partial \phi} \right\} \delta\phi.$$

We note immediately that, if the fields ϕ satisfy the equations of motion, the second term disappears and if the transformation is a symmetry, then we have a conserved quantity, or 4-vector *current*, defined as

$$j^\mu(x) := \frac{\partial \mathscr{L}}{\partial(\partial_\mu \phi)} \delta\phi - \mathscr{J}^\mu \tag{2.2}$$

or, equivalently, the Noether charge

$$Q := \int d^3x\, j^0(x) \tag{2.3}$$

is constant in time.

2.1.2 Scalar and spinor fields

So far, we haven't made any assumption about the fields ϕ appearing in the Lagrangian $\mathscr{L}$ nor about the Lagrangian itself. However, in order to develop the theory we need to specify our Lagrangian. Let's consider two concrete examples: a scalar and a spinor field.

Scalar field The simplest case is to consider a (real) scalar field $\phi(x)$. It obeys the Klein-Gordon equation

$$(\partial^2 + m^2)\phi = 0, \tag{2.4}$$

that can be obtained by applying equation 2.1 to the Lagrangian

$$\mathscr{L}_{KG} = \frac{1}{2}\left[\partial_\mu \phi\, \partial^\mu \phi - m^2 \phi^2\right]$$

where m is the mass of the particle associated with the field. Our objective is to specify a quantum theory for the field, thus we need also to specify the commutation relations for it. This is done by considering the Fourier expansion of the field and its conjugate momentum $\pi(\mathbf{x}) = \frac{\delta \mathscr{L}}{\delta \dot{\phi}}$ (using the notation in [52]):

$$\phi(\mathbf{x}) = \int \frac{d^3k}{(2\pi)^3} \frac{1}{\sqrt{2\omega_k}}\left(a_k e^{i\mathbf{k}\cdot\mathbf{x}} + a_k^\dagger e^{-i\mathbf{k}\cdot\mathbf{x}}\right)$$

$$\pi(\mathbf{x}) = \int \frac{d^3k}{(2\pi)^3} (-i)\sqrt{\frac{\omega_k}{2}}\left(a_k e^{i\mathbf{k}\cdot\mathbf{x}} - a_k^\dagger e^{-i\mathbf{k}\cdot\mathbf{x}}\right)$$

and promoting the Fourier coefficients $a, a^\dagger$ to operators

$$\left[a_p, a_k^\dagger\right] = (2\pi)^3 \delta^{(3)}(\mathbf{p} - \mathbf{k})$$

such that the canonical commutation relation is satisfied (the other commutators are trivial):

$$\left[\phi(\mathbf{x}), \pi(\mathbf{y})\right] = i\delta^{(3)}(\mathbf{x} - \mathbf{y}).$$

The operators a_k and $a_k^\dagger$ are functionally equivalent to the ladder operators for a harmonic oscillator, respectively creating and annihilating the single particle state with momentum $\mathbf{k}$.

Note that in the case of a complex scalar field $\mathscr{L} = \partial_\mu \phi \, \partial^\mu \phi^\dagger - m^2 \phi \phi^\dagger$ the Fourier expansion becomes

$$\phi(\mathbf{x}) = \int \frac{d^3k}{(2\pi)^3} \frac{1}{\sqrt{2\omega_k}} \left(a_k e^{i\mathbf{k}\cdot\mathbf{x}} + b_k^\dagger e^{-i\mathbf{k}\cdot\mathbf{x}} \right). \tag{2.5}$$

Since the field is not Hermitian, the two Fourier coefficients are not correlated and we need to introduce two independent sets of creation and annihilation operators $(a, a^\dagger)$ and $(b, b^\dagger)$. If we then calculate the Noether charge (2.3)

$$Q = \int d^3k \left[a_k^\dagger a_k - b_k^\dagger b_k \right]$$

and have it act on the states created with $a^\dagger$ and $b^\dagger$ acting on vacuum

$$Q \, a^\dagger \left| 0 \right\rangle = +a^\dagger \left| 0 \right\rangle, \qquad Q \, b^\dagger \left| 0 \right\rangle = -b^\dagger \left| 0 \right\rangle$$

we see that the two operators create two particles with opposite charge (but same mass), that we will call respectively *particle* and *antiparticle*. What the field operator $\phi^\dagger$ does then is essentially produce a unit of charge by creating a particle and annihilating an antiparticle, while ϕ acts in the exact opposite way [69].

Dirac spinor   An interesting case arises when we consider the Dirac equation

$$\left(i\gamma^\mu \partial_\mu - m \right)\psi = 0. \tag{2.6}$$

The equation was first formulated by Dirac by trying to write a linear wave equation in both space and time derivatives (as opposed to the Klein-Gordon equation 2.4, quadratic in both space and time). The derivation (see for instance [64] and [69]) implies that the γ^μ cannot be just c-numbers, but four linearly independent matrices with minimum dimension 4×4 satisfying the Clifford algebra:

$$\left\{ \gamma^\mu, \gamma^\nu \right\} = 2\eta^{\mu\nu}$$

where $\eta^{\mu\nu}$ is the metric tensor in Minkowski space and the curl brackets indicate anticommutation. The object $\psi(x)$ is therefore a 4-component *spinor* that must be treated differently from a scalar field. Ideally, we want this object to describe an electron wavefunction, and observations require Pauli exclusion: two electrons cannot have the same quantum numbers, and thus a 2-electron wavefunction should be antisymmetric with respect to quantum number exchange. This translates into the requirement that the creation and annihilation operators satisfy anticommutation relations instead of the canonical commutators. The Fourier expansion is analogous to the one for the complex scalar field 2.5, but

we have to introduce summing over the possible spin indices s and the spinor components of the field $u^s(p)$ and $v^s(p)$:

$$\psi(\mathbf{x}) = \int \frac{d^3 k}{(2\pi)^3} \frac{1}{\sqrt{2E_k}} \sum_s \left(b_k^s u^s(k) e^{i\mathbf{k}\cdot\mathbf{x}} + d_k^{s\,\dagger} v^s(k) e^{-i\mathbf{k}\cdot\mathbf{x}} \right).$$

The creation and annihilation operators must now satisfy (analogously for $d, d^\dagger$)

$$\left\{ b^s(p), b^{r\,\dagger}(k) \right\} = \delta^{(3)}(p-k)\delta_r^s$$
$$\left\{ b^s(p), b^r(k) \right\} = \left\{ b^{s\,\dagger}(p), b^{r\,\dagger}(k) \right\} = 0$$

and this translates into requiring anticommutators for the fields $\psi, \psi^\dagger$ themselves:

$$\left\{ \psi_a(x), \psi_b^\dagger(y) \right\} = \delta^{(4)}(x-y)\delta_a^b$$
$$\left\{ \psi, \psi \right\} = \left\{ \psi^\dagger, \psi^\dagger \right\} = 0.$$

Note that a bi-linear object such as $\psi\psi^\dagger$ is not Hermitian (fact that follows from the signature of Minkowski metric), and therefore for calculations it is useful to restore Hermiticity by defining the object

$$\bar{\psi} := \psi^\dagger \gamma^0$$

where γ^0 is the first and only Hermitian of the gamma matrices. The Dirac lagrangian, leading to the Dirac equation of motion 2.6 reads then, with the short-hand $\gamma^\mu \partial_\mu = \slashed{\partial}$

$$\mathscr{L}_D := \bar{\psi}\left(i\slashed{\partial} - m \right)\psi. \tag{2.7}$$

As a final remark it is interesting to point out the action of those operators on the vacuum $|0\rangle$: $b_p^{s\dagger}$ creates a state with spin s and momentum $\mathbf{p}$. If we act with another creation operator $b_k^{r\dagger}$, the anticommutators above are simply

$$b_p^{s\dagger} b_k^{r\dagger} |0\rangle = -b_k^{r\dagger} b_p^{s\dagger} |0\rangle \,,$$

i.e. the two-particle wavefunction is antisymmetric under particle exchange. Therefore particles described by those objects (defined to explain the behaviour of spin-1/2 particles) obey Fermi-Dirac statistics [52]. This comes from a more general result, known as spin-statistics theorem, first formulated by Pauli [50, 49]: under the hypotheses that causality is preserved (all trajectories are confined inside the light-cone), the expressions are Lorentz-invariant, and the norms in Hilbert spaces are positive. Particles with integer spin obey Bose-Einstein statistics, whereas particles with half-integer spin obey Fermi-Dirac statistics.

2.1.3   Discrete symmetries

Discrete symmetries in physics allow us to make general statements but also can offer some insights in Beyond the Standard Model (BSM) Physics when we consider scenarios in which those are violated. Here we are going to introduce parity, charge conjugation and time-reversal symmetries, discuss their role in SM theories and end with stating the general result of CPT theorem, probably one of the most fundamental conservation laws.

Parity   Parity transformation is essentially a spatial reflection, i.e. the inversion of the spatial component in our spacetime coordinates:

$$P\psi(x^0, \mathbf{x}) = \psi(x^0, -\mathbf{x}).$$

Note that by acting on ψ with P two times we obtain the original wavefunction, and thus $P^2 = 1$ with eigenvalues ± 1. The γ^0 matrix (in Weyl representation) satisfies this requirement and it is possible to show that, if we define our transformed object

$$\psi'(x') := \gamma^0 \psi(x)$$

up to an arbitrary phase, then it satisfies Dirac equation in the transformed coordinates $x' = (x^0, -\mathbf{x})$ [69]. Thus we can just identify the parity operator P acting on a Dirac spinor with the γ^0 matrix

$$P\psi(x) \equiv \gamma^0 \psi(x). \tag{2.8}$$

Note that, depending on their behaviour under P transformations and Lorentz transformations we can define different Dirac bilinears, listed in table 2.1 where we have introduced the matrix $\gamma^5 = i\gamma^0 \gamma^1 \gamma^2 \gamma^3$.

		P
scalar	$\bar{\psi}\psi$	1
pseudoscalar	$\bar{\psi}\gamma^5\psi$	-1
vector	$\bar{\psi}\gamma^\mu\psi$	$(-1)^\mu$
axial vector	$\bar{\psi}\gamma^5\gamma^\mu\psi$	$-(-1)^\mu$

Table 2.1: Principal Dirac bilinears and their behaviour under parity transformation.

Charge conjugation   The effect of charge conjugation C is mapping a fermion with spin orientation s into an antifermion with the same spin orientation

$$Cb_p^s C = d_p^s \qquad Cd_p^s C = b_p^s.$$

Note that also in this case the operator is unitary, as acting twice on the fermion with C we get the same fermion. If we compute the action of C on the fields [52] we obtain

$$C\psi(x)C = -i\gamma^2(\psi^\dagger)^T = -i(\bar{\psi}\gamma^0\gamma^2)^T$$

and, if we define the field

$$\psi_c := C\gamma^0\psi^* = \gamma^2\psi^*, \tag{2.9}$$

it is possible to show that ψ_c satisfies the Dirac equation 2.6 [69], thus describing a field with the same mass as ψ, but opposite charge (because of the complex conjugate). This is indeed the way to relate ordinary fermionic matter to antimatter, and we will make use of it in the next section, where we will discuss Majorana particles.

Time reversal   The last discrete symmetry we will discuss is time reversal T, essentially the flipping of the time axis of our trajectory

$$b_p \to b_{-p}, \qquad \psi(t, \mathbf{x}) \to \psi(-t, \mathbf{x}).$$

It can be shown [52] that we cannot express it as a linear unitary operator, and we have to drop the unitarity requirement. The result is that our operator T is antiunitary and not only reverses the particle momentum, but also its spin. Thus its action on the fermion operators is

$$Tb_p^s T = b_{-p}^{-s} \qquad Td_p^s T = d_{-p}^{-s}$$

and on the fields

$$T\psi(t, \mathbf{x})T = \gamma^1\gamma^3\psi(-t, \mathbf{x}). \tag{2.10}$$

As a final remark, we should note that these are all symmetries of the free Dirac theory, but can in principle be violated once we consider interactions between fermions. In fact, violation of CP symmetries are not only allowed by the theory of the weak interaction, but have also been precisely measured in the quark sector [10, 2, 1]. CP violation and its phenomenology will indeed be a *leitmotiv* throughout this thesis.

However, note that if we consider the combined actions of 2.9, 2.8 and 2.10, we just get an overall γ factor in front of our spinor. This factor has our theory now describe an antifermion, not a fermion, and hints at a very fundamental symmetry between matter and antimatter [60]. Indeed a very general result, known as the CPT theorem, states that any local field theory which is Lorentz invariant and preserves causality is invariant under CPT (intended as the combined action of 2.9, 2.8 and 2.10) [52, 69]. Under stronger hypotheses, it is even possible to show that if CPT symmetry is violated, then Lorentz invariance is violated as well.

Chirality   Another concept that is useful to introduce is chirality. If we introduce the left- an right-handed operators defined respectively as

$$P_{L,R} := \frac{1}{2}\left(1 \mp \gamma^5\right), \tag{2.11}$$

it is possible to decompose a field ψ into its right- and left-handed component, or Weyl spinors:

$$\psi(x) = \psi_L(x) + \psi_R(x) = P_L\psi(x) + P_R\psi(x)$$

and, if we use this decomposition in the Dirac lagrangian 2.7, we obtain

$$\mathscr{L} = i\bar{\psi}_L \slashed{\partial}\psi_L + i\bar{\psi}_R \slashed{\partial}\psi_R - m(\bar{\psi}_l\psi_R + \bar{\psi}_R\psi_L). \tag{2.12}$$

We note immediately that the mass term couples the left-handed and right-handed Weyl spinors, with the effect of mixing chirality. If this is the case $\mathscr{L}$ would also be invariant under $\psi \to e^{i\phi\gamma^5}\psi$ (where ψ is an arbitrary phase), and the axial current $j^\mu \equiv \bar{\psi}\gamma^\mu\gamma^5\psi$ would be a constant in the motion.

Chirality is fundamental in understanding the mechanism of the weak interactions, whose vertex includes a P_L factor. Thus this allows for parity violation, as the charged weak bosons only couple to left-handed fermions (and right-handed antifermions), while parity reverses the handedness of a fermion.

2.1.4   Interactions: Gauge invariance and Yang-Mills theories

Another symmetry possessed by the free Dirac Lagrangian 2.7 is invariant under the transformation of the field with a global arbitrary phase factor

$$\psi(x) \to e^{i\alpha}\psi(x).$$

We want however to introduce a stronger constraint, and require local invariance instead

$$\alpha = \alpha(x).$$

To obtain this we need to compensate for the extra term appearing when the derivative operator acts on the local phase $\alpha(x)$, by defining the *covariant derivative*

$$D_\mu := \partial_\mu + ieA_\mu(x)$$

and replacing the derivative operator in 2.7 with it. Note that we are forced to introduce the vector field $A_\mu(x)$ and require it to transform as

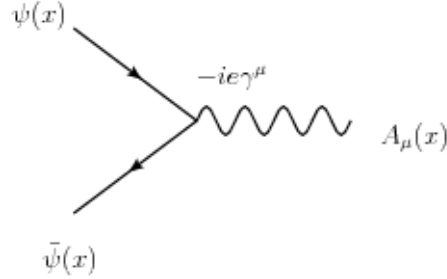$$A_\mu(x) \to \tilde{A}_\mu(x) \equiv A_\mu - \frac{1}{e}\partial_\mu\alpha$$

Figure 2.1: QED vertex describing the coupling of the photon to fermions.

once we apply the local transformation to the field ψ. This is exactly the gauge invariance requirement for an electromagnetic field [38].

We have essentially just introduced the photon in the Dirac Lagrangian, by just requiring local gauge invariance for the Dirac field ψ. The covariant derivative specifies in a natural way the coupling of the "new" gauge boson with the fermion fields, by introducing in the Lagrangian term

$$\mathscr{L} \supset ie\bar{\psi}\gamma^\mu A_\mu \psi$$

corresponding to the fundamental QED vertex in figure 2.1.

This procedure can in principle be generalized to derive other gauge-invariant theories. Let us now consider multiplets of fermion fields

$$\Psi := \begin{bmatrix} \psi_1 \\ \dots \\ \psi_n \end{bmatrix}$$

grouped together because they show similar properties with respect to some interactions. Let us also introduce a continuous group of transformations G, where an element $V \in G$ is a unitary matrix that can be written as a (infinite) sum of infinitesimal transformations

$$\Psi \to V\Psi, \qquad V\Psi = e^{i\alpha^a t^a}\Psi \tag{2.13}$$

where α^a are coefficients and $\{t^a\}_a$ the generators of the group. Note that the Hermiticity of the generators implies unitarity of the matrix V.

As before, the free lagrangian $\bar{\Psi}(i\slashed{\partial} - m)\Psi$ is globally invariant under 2.13, and we require local invariance. This means that we should introduce once again the covariant derivative

$$D_\mu \equiv \partial_\mu - igA_\mu^a(x)t^a$$

where we have introduced one vector field $A_\mu^a(x)$ for each generator. Thus, the covariant derivative is not specified if the symmetry group is not specified.

Considering infinitesimal transformations $\Psi \rightarrow (1 + i\alpha^a t^a)\Psi$ (we can do this since the group G is continuous and each element can be reached with a series of infinitesimal transformations), it is possible to show [52] that our vector bosons transform as

$$A_\mu^a \rightarrow A_\mu^a + \frac{1}{g}\partial_\mu \alpha^a + f^{abc}A_\mu^b \alpha^c$$

where we have defined $f^{abc} := i[t^c, t^b]t^a$, the structure constants of the group. Note that non-zero structure constants define a non-abelian group, unlike the case of the photon, worked out before.

We can almost write a general Lagrangian for any general multiplet Ψ, but first we have to define a mass term for the newly introduced vector fields. Since terms like $\sim A_\mu A^\mu$ are not gauge invariant, the only term we can add (up to mass-dimension 4 and respecting P,T invariance) is the field tensor $F_{\mu\nu}$ defined considering the commutator of the covariant derivative

$$[D_\mu, D_\nu] = -igF_{\mu\nu}^a t^a.$$

Writing it explicitly we obtain

$$F_{\mu\nu}^a = \partial_\mu A_\nu^a - \partial_\nu A_\mu^a + gf^{abc}A_\mu^b A_\nu^c.$$

We can see that this term does not only specify the propagation of the free gauge bosons, but also -if the theory is non-abelian- the self interactions, i.e. the couplings of the gauge boson with itself. This is for instance true in quantum chromodynamics (QCD), describing the interactions of quarks, and in the theory of electroweak interactions.

At this point we have all the elements to write the most general lagrangian describing a quantum field theory, the Yang-Mills lagrangian:

$$\mathscr{L}_{YM} \equiv \bar{\Psi}(i\slashed{D} - m)\Psi - \frac{1}{4}(F_{\mu\nu}^a)^2.$$

Note that this lagrangian is completely specified only once we define the group of transformations under which we require local gauge invariance. Thus specifying the symmetry group is effectively equivalent to specifying the theory describing our fields.

2.1.5 The Standard Model

It appears, to the day, that Nature has chosen three symmetry groups to describe the fundamental interactions of matter:

$$U(1)_Y \otimes SU(2)_L \otimes SU(3)_C.$$

- $U(1)_Y$: unitary transformations acting on Yang-Mills singlets described by the hypercharge Y, related to the electromagnetic charge Q by $Q = I_3 + \frac{1}{2}Y$ where I_3 is the third component of isospin introduced below. It has one generator, describing QED interactions.

- $SU(2)_L$: unitary transformations U such that $\det(U) = 1$, acting on left-handed fermionic isospin doublets $I = \frac{1}{2}$, $I_3 = \pm\frac{1}{2}$. It has three generators, describing the weak interactions of leptons and quarks.

- $SU(3)_C$: unitary transformations acting on quark color triplets $c = r, g, b$. It has 8 generators, corresponding to all the possible gluons of QCD interactions.

These three symmetry groups, together with three generations of fermions (usually arranged in isospin doublets), are the fundamental ingredients for the quantum field theory known as the Standard Model of elementary particles (figure 2.2). It is probably the most predictive and well-verified theory in the history of Physics, but it is not perfect: it fails, for instance, to provide a quantum description for gravity. This and other issues, such as the lack of an explanation for why there are three generations of quarks and leptons, or the violation of CP symmetry to list just some, open the research towards extending the theory and searching for beyond the standard model (BSM) phenomena.

A first remark considers the isospin singlets $I = 0$, describing (left-)right-handed (anti)fermions. A null isospin means that the weak gauge bosons do not couple to those particles and thus parity is maximally violated. If the fermion has also neutral charge Q, then it does not couple to the QED gauge boson, and thus is expected not to interact with matter at all. This is the case for the right-handed neutrinos, which because of their sterile behaviour can be essentially excluded from the theory.

Secondly, the bosons associated to $U(1)_Y \otimes SU(2)_L$ are not the physical bosons we detect in the laboratory. The explanation for this comes from the Glashow-Weinberg-Salam model [35, 67, 61], and is related to a non-zero vacuum expectation value. The actual physical bosons $A, W^\pm$ and Z^0 are linear combinations of the states introduced with the symmetry groups. Furthermore, those states are initially massless, but once the $U(1)_Y \otimes SU(2)_L$ symmetry is broken mass appears as an extra degree of freedom arising from the generation of a Goldstone boson through the Higgs (BEH) mechanism [29, 39].

Lastly, the mass term we have been writing in the Dirac lagrangian is actually not gauge invariant, and the Standard Model being a gauge-invariant theory actually predicts massless bosons. Their mass is indeed the result of their coupling with a scalar field, the Higgs field, which introduces mass-like terms in the full Lagrangian. Those terms are actually the ones that we have been writing with some abuse of notation as m throughout the whole section. One final caveat: the Higgs mechanism with the coupling to the Higgs field is able to elegantly explain the origin of fermion masses, however new physics is needed to explain neutrino masses (see next section) since a standard mass term implies the existence of a right handed neutrino, which has not been experimentally detected yet.
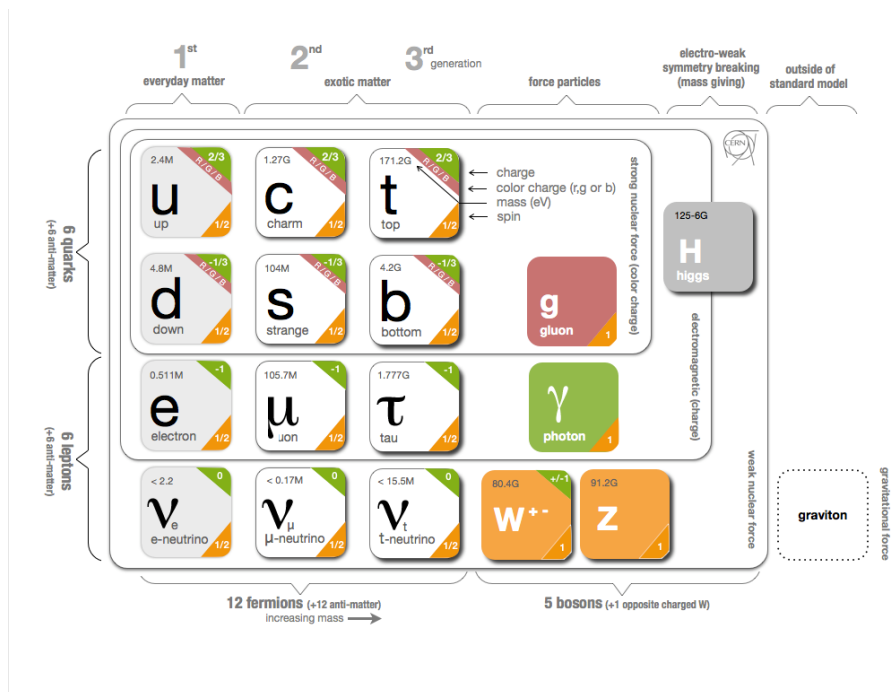
Figure 2.2: Schematic representation of the fermionic and bosonic fields included in the Standard Model. From `http://united-states.cern/physics/standard-model-and-beyond`

2.2 Overview of neutrino physics

Neutrinos are the upper component of the leptonic isospin doublets. Until recently they were assumed to be massless in the Standard Model. However, this proved not to be the case with the measurement of neutrino oscillations [32, 5]. Since then interest around neutrino physics has steadily grown, but a lot of questions still need to be answered: what are the values of their masses, are they Dirac or Majorana particles and whether or not CP symmetry is violated in neutrino interactions are probably the most discussed topics to the day. We present here an overview of these phenomena.

2.2.1 Neutrino oscillations

Neutrino oscillations arise from the fact that there is no full overlap between the mass eigenstates of the free-propagating hamiltonian

$$\hat{H}\psi = E\psi, \qquad \psi(t, \mathbf{x}) = e^{iEt}\phi(\mathbf{x})$$

and the weak eigenstates produced together with the correspondent lepton in a weak interaction. If we label (ν_1, ν_2, ν_3) and $(\nu_e, \nu_\mu, \nu_\tau)$ respectively, they are linked together with a linear superposition of states defined by the 3×3 PMNS unitary matrix U, named after the work of Pontecorvo and Maki-Nakagawa-Sakata [54, 46]:

$$\begin{bmatrix} \nu_1 \\ \nu_2 \\ \nu_3 \end{bmatrix} = \begin{bmatrix} U_{e1} & U_{e2} & U_{e3} \\ U_{\mu1} & U_{\mu2} & U_{\mu3} \\ U_{\tau1} & U_{\tau2} & U_{\tau3} \end{bmatrix} \begin{bmatrix} \nu_e \\ \nu_\mu \\ \nu_\tau \end{bmatrix}. \tag{2.14}$$

If for instance a muon neutrino is produced in a weak interaction vertex $(t, \mathbf{x}) = (0, \mathbf{0})$, its wavefunction will be a superposition of mass eigenstates

$$|\psi(0, \mathbf{0})\rangle = |\nu_\mu\rangle = U_{\mu1}^* |\nu_1\rangle + U_{\mu2}^* |\nu_2\rangle + U_{\mu3}^* |\nu_3\rangle.$$

Its time evolution is described essentially as the mass eigenstates propagating as plane waves, and thus each obtaining the phase factor $e^{-i\phi_i}$ for $i = 1, 2, 3$, where $\phi_i := (p_\mu x^\mu)_i = E_i t - \mathbf{p} \cdot \mathbf{x}$. Note that, since neutrinos are detected only in a weak interaction where a charged lepton is produced, it is convenient to express the mass eigenstates directly in terms of the weak eigenstates. This leads to

$$\begin{aligned} |\psi(t, \mathbf{x})\rangle = & \left[U_{e1}^* U_{e1} e^{-i\phi_1} + U_{e2}^* U_{e2} e^{-i\phi_2} + U_{e3}^* U_{e3} e^{-i\phi_3} \right] |\nu_e\rangle \\ & + \left[U_{\mu1}^* U_{\mu1} e^{-i\phi_1} + U_{\mu2}^* U_{\mu2} e^{-i\phi_2} + U_{\mu3}^* U_{\mu3} e^{-i\phi_3} \right] |\nu_\mu\rangle \\ & + \left[U_{\tau1}^* U_{\tau1} e^{-i\phi_1} + U_{\tau2}^* U_{\tau2} e^{-i\phi_2} + U_{\tau3}^* U_{\tau3} e^{-i\phi_3} \right] |\nu_\tau\rangle. \end{aligned}$$

The probability of detecting the state ν_α ($\alpha = e, \mu, \tau$) at coordinates $(t, \mathbf{x})$ is then

$$P(\nu_\mu \to \nu_\alpha) = |\langle \nu_\alpha | \psi(t, \mathbf{x}) \rangle|^2 = |U_{\mu1}^* U_{\alpha1} e^{-i\phi_1} + U_{\mu2}^* U_{\alpha2} e^{-i\phi_2} + U_{\mu3}^* U_{\alpha3} e^{-i\phi_3}|^2. \tag{2.15}$$

It is clear at this point that if the phase factors were all the same, then the probability to detect a different state at a different point in space and time would be null, since the matrix U is unitary and the weak eigenstates are, by definition, orthonormal. Thus neutrino oscillations can only be detected if neutrino masses are not only non-zero, but also different from each other (and this is indeed the case).

2.2.2 Neutrino masses and mass hierarchy

If we continue working on equation 2.15 and we consider, for instance, the muon neutrino survival probability $P(\nu_\mu \to \nu_\mu)$, we can arrive at an expression [64] of the form

$$P(\nu_\mu \to \nu_\mu) = 1 - 4|U_{\mu 1}|^2|U_{\mu 2}|\sin^2\Delta_{21} - 4|U_{\mu 1}|^2|U_{\mu 3}|\sin^2\Delta_{31}$$
$$- 4|U_{\mu 2}|^2|U_{\mu 3}|\sin^2\Delta_{32}$$

where we have introduced the oscillation parameter

$$\Delta_{ij} := \frac{\phi_j - \phi_i}{2} = \frac{m_j^2 - m_i^2}{4}\frac{L}{E_\nu}.$$

The first thing we should notice is that the period of the oscillation scales with the ratio $\frac{E_\nu}{L}$. This means that, adjusting the energy of a potential neutrino beam, it is possible to collect data comparable, for instance, to solar neutrinos. Furthermore, the survival probability depends on the difference between the squared masses $\Delta m_{ij}^2 \equiv m_i^2 - m_j^2$. Of these differences, only two are independent while the third one can be written as the sum of the other two:

$$\Delta_{31} = \Delta_{32} + \Delta_{21}.$$

Results from solar neutrinos show that Δm_{21}^2 is positive [36], but the sign of Δm_{32}^2, coming from atmospheric neutrino data, is still to be determined. This is commonly known as the neutrino mass hierarchy problem [57] and basically consists of determining whether ν_3 is heavier or lighter than the ν_1 and ν_2 mass eigenstates. The former hypothesis is referred to as *normal hierarchy*, while the latter is called *inverse hierarchy*, reflecting the weak eigenstates component content in each state. Figure 1.3 in Chapter 1 illustrates the two possible mass splitting hypotheses.

   To the day, we do not have sensitive enough experiments to provide an answer to this problem, since we are not really sensitive to the $1-3$ component of the oscillation probabilities, and no direct measurements of neutrino masses have been performed. For the latter, cosmological arguments can provide a constraint on an upper limit, since the density of freezed-out neutrino relics after the Big Bang is rather high (113cm^{-2}[51]). Even though it varies depending on the model chosen, we will report the value from [53] obtained by combining cosmic microwave background and baryonic acoustic oscillation data, according

to which the sum of the masses of the three mass eigenstates

$$\sum_{i=1}^{3} m_1 < 0.23\text{eV}.$$

The tightest experimental limit up to now is the one obtained from KATRIN in 2019 [6], that sets the neutrino mass scale to

$$m_\nu < 1.1\text{eV}.$$

2.2.3 Dirac or Majorana

During our discussion about chirality, we expressed the Dirac lagrangian 2.12 in term of the chiral eigenstates ψ_L and ψ_R. If we use it to derive the equations of motion for those two fields we get to

$$i\slashed{\partial}\psi_L = m\psi_R$$
$$i\slashed{\partial}\psi_R = m\psi_L$$

where the two degrees of freedom are coupled by the mass term. We want to see now if it is possible to write similar equations in terms of a single decoupled degree of freedom. To do that we should introduce the charge conjugation operator 2.9 and require the right-handed component to be

$$\psi_R \overset{!}{=} C\bar{\psi}_L^T \equiv \psi_L^c.$$

It is possible to show that indeed, the result of this operation is a right-handed field [17]. The field ψ will now become

$$\psi = \psi_L + \psi_R = \psi_L + \psi_L^c$$

and if we consider its charge conjugate

$$\psi^c = \left(\psi_L + \psi_L^c\right)^c = \psi_L^c + \psi_L = \psi,$$

implying that the charge conjugate of the field is the field itself or, equivalently, that the particle described by ψ is its own antiparticle.

This allows us to write two decoupled *Majorana* equations of motion,

$$i\slashed{\partial}\psi_L = m\psi_L^c$$
$$i\slashed{\partial}\psi_R = m\psi_R^c$$

with two independent degrees of freedom. It is important to point out that such a procedure can be derived only if the charge of the fermions is 0, otherwise the charge conjugation will introduce a $-$ sign and the derivation would not hold. For this reason neutrinos are ideal candidates to be Majorana fermions.

Note that a Dirac-like term implies the existence of a right-handed component of the spinor doublet, i.e. the existence of a sterile right-handed neutrino is required in the Standard Model to explain (left-handed)neutrino interactions. A Majorana-like term effectively decouples the two degrees of freedom and does not require the presence of both fermions.

Seesaw mechanism   These considerations allow us to write two new Lorentz-invariant mass terms

$$\sim m_L \bar{\psi}_L \psi_L^c, \qquad \sim m_R \bar{\psi}_R \psi_R^c \qquad + h.c.$$

with two different mass-like factors since the terms are independent. The most general mass Lagrangian we can write, including also Dirac terms, is

$$\mathscr{L} \supset m_D \bar{\psi}_R \psi_L + m_D \bar{\psi}_L \psi_R + m_L \bar{\psi}_L \psi_L^c + m_R \bar{\psi}_R \psi_R^c + h.c.$$

where m_D is the mass factor of the Dirac terms. This expression can be written in matrix form as

$$\mathscr{L} \supset \begin{bmatrix} \bar{\psi}_L^{\;c} & \bar{\psi}_R \end{bmatrix} \begin{bmatrix} m_L & m_D \\ m_D & m_R \end{bmatrix} \begin{bmatrix} \psi_L \\ \psi_R^c \end{bmatrix} + h.c.$$

Now, since the mass matrix

$$M := \begin{bmatrix} m_L & m_D \\ m_D & m_R \end{bmatrix}$$

is not diagonal, the chiral eigenstates ψ_L, ψ_R^c do not correspond to the physical mass eigenstates ψ_L^1, ψ_L^2, and in order to determine the latter we need to diagonalize the matrix M. If we assume the components of M to satisfy $m_L = 0, m_D \ll m_R$ [64, 17], this leads to the prediction of a light neutrino state

$$\nu \simeq (\psi_L + \psi_L^c) - \frac{m_D}{m_R}(\psi_R + \psi_R^c) \qquad \text{with mass } m_\nu \simeq \frac{m_D^2}{m_R}$$

and a heavy neutrino state

$$N \simeq (\psi_R + \psi_R^c) + \frac{m_D}{m_R}(\psi_L + \psi_L^c) \qquad \text{with mass } m_\nu \simeq m_R.$$

In other words, for each light neutrino state ν with mass much smaller than the Standard Model fermions, there is a considerably heavy neutrino state N. However, for this to be the case, its mass is expected to be of the order of 10^{11} GeV.

Of course, for this to be the case we need to verify that neutrinos actually are Majorana fermions. The most promising process to look for in this context is neutrinoless double-beta decay, shown in figure 2.3, where the two antineutrinos produced from the decay of two nuclear neutrons annihilate each other and in the final state only two electrons appear. However, the lifetime for this process is expected to be $\gtrsim 10^{28}$ years [20], and thus being able to detect enough of such events proves to be an experimental challenge.
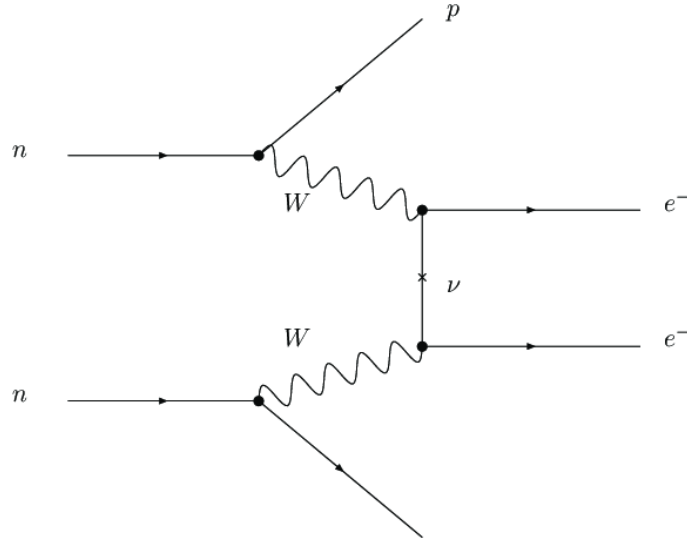
Figure 2.3: Feynman diagram for neutrinoless double-beta decay.

2.3 CP violation

2.3.1 Baryogenesis and Sakharov conditions

In most models for nucleosynthesis it is usually assumed that in the universe the photon density is higher than the baryon density by orders of magnitude. This is a reasonable statement if we consider that at low temperatures baryons and antibaryons will annihilate each other. However, this does not explain why we are able to detect baryons and why there are baryons at all. At the very high thermal background temperature kT of the early universe net charge neutrality implies that there is an equal number of protons and antiprotons, and the symmetry is mantained when the species annihilate. After freeze-out processes we should be able to detect a low abundance of both species, but this is not the case: the universe does not display a symmetry between matter and antimatter. The reason for this is the existence of a slight asymmetry in the early universe, where for each antiproton there are $1+O(10^9)$ protons [51]. This can then be set as initial condition and cannot be modified, as long as baryon number B is conserved.

The C violation in the Universe can happen as long three conditions, first stated by Sakharov in an article published in 1967 [59], are respected:

1. *Direct B violation.* A violation in baryon number conservation means that the distinction between baryons and leptons is erased. This can be explained in the framework of Grand-Unified Theories (GUTs) -for

instance SU(5) [34], which allow for decays of a X boson such as

$$X \to e^+ + \bar{d}. \tag{2.16}$$

This would imply the possibility of transitions between baryons and leptons, and decay processes such as a proton decaying as

$$p \to e^+ \pi^0.$$

However, given that a proton is a very stable particle, the mass of such X boson is expected to be very large. However, this processes could have happened in the very early universe, when kT was high enough such that the GUT symmetry was not broken.

2. *CP violation.* Asymmetry between particles and antiparticles is required. This means that if we consider processes such as 2.16 and its charge conjugate

$$\bar{X} \to e^- + d, \tag{2.17}$$

the branching ratio for the two decays is different. Such difference has been measured in laboratory for the system of neutral kaons, discussed in the next section, and B-mesons.

3. *Non-equilibrium.* This condition essentially prevents reactions from cancelling the asymmetry once it has been created. The crucial physical result relies then in the ability of the reaction to successively freeze out.

2.3.2 CP violation in quark sector

Flavour mixing and CKM matrix A phenomenon analogous to neutrino mixing described by 2.14 happens for the weak interactions of quarks, where there is no direct correspondence between the weak (d', s', b') and mass (d, s, b) eigenstates. This hypothesis was first introduced by Cabibbo [19] with a 2D rotation matrix governed by the mixing Cabibbo angle θ_c, and later extended to the three quark flavours with the unitary Cabibbo-Kobayashi-Maskawa (CKM) matrix V

$$\begin{bmatrix} d' \\ s' \\ b' \end{bmatrix} = \begin{bmatrix} V_{ud} & V_{us} & V_{ub} \\ V_{cd} & V_{cs} & V_{cb} \\ V_{td} & V_{ts} & V_{tb} \end{bmatrix} \begin{bmatrix} d \\ s \\ b \end{bmatrix}.$$

This matrix can be described as the effect of three rotations $\theta_{12}, \theta_{13}, \theta_{23}$ and a complex phase δ, that takes into account potential CP violations

$$V = \begin{bmatrix} 1 & 0 & 0 \\ 0 & c_{23} & s_{23} \\ 0 & -s_{23} & c_{23} \end{bmatrix} \begin{bmatrix} c_{13} & 0 & s_{13}e^{-i\delta} \\ 0 & 1 & 0 \\ -s_{13}e^{-i\delta} & 0 & c_{13} \end{bmatrix} \begin{bmatrix} c_{12} & s_{12} & 0 \\ -s_{12} & c_{12} & 0 \\ 0 & 0 & 1 \end{bmatrix} \tag{2.18}$$

where we have introduced the short-hand notation $s_{ij} := \sin\theta_{ij}$, $c_{ij} := \cos\theta_{ij}$. Since the matrix is quasi-diagonal [68], it is customary to approximate it to $O(\lambda^4)$ as an expansion of the small parameter $\lambda := \sin\theta_c$, and express it in terms of the four real Wolfenstein parameters λ, A, ρ, η:

$$
V = \begin{bmatrix} 1 - \frac{\lambda^2}{2} & \lambda & A\lambda^3(\rho - i\eta) \\ -\lambda & 1 - \frac{\lambda^2}{2} & A\lambda^2 \\ A\lambda^3(1 - \rho - i\eta) & -A\lambda^2 & 1 \end{bmatrix} + O(\lambda^4). \tag{2.19}
$$

Neutral Kaons The first evidence of CP violation comes from the measurements of neutral kaon decays by Cronin and Fitch [21]. The neutral kaons $K_0(s\bar{s})$ and $\bar{K}_0(s\bar{d})$ are the lightest meson states with strangeness, and because of this kinematics allow only the weak decay into pions or e^-, μ^-, ν. The other important feature is that the weak interaction allows also the processes shown in figure 2.4 allowing for $K_0 \leftrightarrow \bar{K}_0$ mixing. Because of this, the physical kaon state has to be considered a linear combination of K_0 and $\bar{K}_0$ states, and we can use the different measured lifetimes to label a short-lived $|K_S\rangle$ and a long-lived $|K_L\rangle$ state [64].

It is also possible to introduce the CP eigenstates, defined as

$$
|K_1\rangle := \frac{1}{\sqrt{2}}\big(|K_0\rangle + |\bar{K}_0\rangle\big) \qquad CP|K_1\rangle = +|K_1\rangle
$$

$$
|K_2\rangle := \frac{1}{\sqrt{2}}\big(|K_0\rangle - |\bar{K}_0\rangle\big) \qquad CP|K_2\rangle = -|K_2\rangle.
$$

If we now restrict ourselves to considering only the decays into pions, we should
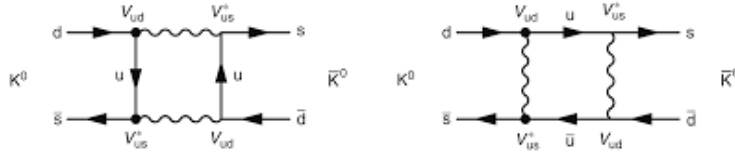

Figure 2.4: Box diagrams for kaon oscillations.

first compute the CP effect on the possible final states, with either two or three pions. It is possible to show [64] that the result is

$$
CP(\pi^0\pi^0) = CP(\pi^+\pi^-) \equiv CP(\pi\pi) = 1
$$

$$
CP(\pi^0\pi^0\pi^0) = CP(\pi^0\pi^+\pi^-) \equiv CP(\pi\pi\pi) = -1
$$

Thus, if CP is conserved, the only allowed decays are

$$
K_1 \to \pi\pi, \qquad K_2 \to \pi\pi\pi.
$$

If we then consider the kinematics, we see that the phase space for the decay into three pions $m(K) - 3m(\pi) \sim 80\text{MeV}$ is considerably smaller than the one for the decay into two pions $m(K) - 2m(\pi) \sim 220\text{MeV}$, and thus we are lead to identify the states

$$|K_1\rangle \equiv |K_S\rangle, \qquad |K_2\rangle \equiv |K_L\rangle.$$

However, the state K_2 is observed to decay in a small fraction of 2-pion final states [21], and thus there must be a violation in the CP symmetry. This violation of the CP symmetry can be introduced in two possible ways:

i. The short- and long-lived states K_S and K_L are not directly identified with the CP eigenstates K_1 and K_2, but rather they are a combination of the latter:

$$|K_{S,L}\rangle = \frac{1}{\sqrt{1 + |\epsilon|^2}} \left(|K_{1,2}\rangle + \epsilon |K_{2,1}\rangle \right)$$

where we have introduced the small mixing parameter $\epsilon \ll 1$. The measured value in kaon systems is $|\epsilon| = (2.228 \pm 0.011) \times 10^{-3}$[63].

ii. Direct CP violation: the long-lived state K_L actually coincides with the odd-CP state K_2, and the violation happens when K_L decays, this time either in a 2- or 3-pion final state. We can quantify this direct violation by considering the ratio

$$\epsilon' := \frac{\Gamma(K_L \to \pi\pi)}{\Gamma(K_L \to \pi\pi\pi)}$$

where Γ is the branching ratio relative to a process.

The ratio between the two parameters has been measured to be [4]

$$\mathbb{R}e\left\{\frac{\epsilon'}{\epsilon}\right\} = (19.2 \pm 2.1) \times 10^{-4}$$

implying that the main contribution to CP violation in the kaon system comes from the $K_0 \leftrightarrow \bar{K}_0$ mixing.

It is also possible to show that

$$|\epsilon| \propto \eta(1 - \rho + \text{const.})$$

thus relating the ϵ parameter to the Wolfenstein matrix elements. Clearly, a non-zero ϵ implies that two elements of 2.19 are complex, and thus the complex phase in 2.18 has to be included in order to account for CP violation.

Similar effects have been measured also for B_0 meson systems, where we can define a heavy B_H^0 and a light B_L^0 state, in the BaBar and Belle experiments [10, 2]. The magnitude of the elements in the CKM matrix is currently well constrained and understood.

2.3.3 CP violation and PMNS matrix

In the leptonic sector searches for CP violation can be conduced with reference to the PMNS matrix 2.14. As for the CKM matrix, it is possible to decompose in terms of three rotation angles $\theta_{12}, \theta_{13}, \theta_{23}$ and six phases, which can be factored out leaving only one single phase δ [64], resulting in

$$
U = \begin{bmatrix} 1 & 0 & 0 \\ 0 & c_{23} & s_{23} \\ 0 & -s_{23} & c_{23} \end{bmatrix} \begin{bmatrix} c_{13} & 0 & s_{13}e^{-i\delta} \\ 0 & 1 & 0 \\ -s_{13}e^{-i\delta} & 0 & c_{13} \end{bmatrix} \begin{bmatrix} c_{12} & s_{12} & 0 \\ -s_{12} & c_{12} & 0 \\ 0 & 0 & 1 \end{bmatrix} \tag{2.20}
$$

where, as before, $s_{ij} := \sin\theta_{ij}$, $c_{ij} := \cos\theta_{ij}$.

At this point, signs of CP violation can be found by considering the difference in oscillation probabilities between neutrinos and antineutrinos:

$$
P(\nu_\mu \to \nu_e) \simeq \sin^2(2\theta_{13}) \sin^2\theta_{23} \sin^2\left(\frac{1.27\Delta m_{32}^2 L}{E}\right)
$$
$$
\mp \frac{1.27\Delta m_{21}^2 L}{E} 8 J_{CP} \sin^2\left(\frac{1.27\Delta m_{32}^2 L}{E}\right)
$$

where we have introduced the Jarlskog invariant [40]

$$
J_{CP} = \frac{1}{8}\cos\theta_{13}\sin(2\theta_{12})\sin(2\theta_{23})\sin(2\theta_{13})\sin\delta
$$

as a basis-independent way to measure the CP phase δ. The minus sign refers to neutrino oscillations, whereas the plus sign describes antineutrino oscillations.

Recent results from T2K [23] have excluded with 95% confidence CP-conserving phases $\delta = 0, \pi$ and have provided the values (with 1σ uncertainties)

$$
\delta^{\text{normal}} = -1.89^{+0.70}_{-0.58}, \qquad \delta^{\text{inverted}} = -1.38^{+0.48}_{-0.54}
$$

depending on whether the normal or inverted mass hierarchy is assumed. There also appears to be a preference for the normal mass ordering. This is an important step as it is the first constraint we have on leptonic CP violation. However, more precision and better resolution are needed in order to rule out with enough confidence the $\delta = 0$ hypothesis. Note also that the determination of δ would also give further insights to explain leptogenesis. This is in fact associated to the decay of a heavy Majorana neutrino into a Higgs - lepton final state, whose Yukawa coupling term is proportional to the PMNS matrix elements [44].

2.4 Outreach potential of ESSνSB

In the context of aiming towards better detection resolution we find the Neutrino Super Beam experiment at ESS. The proposal arises from the measurement of a rather large mixing angle $\theta_{13} \sim 8°$, that opened the possibility to measure leptonic CP violation from neutrino oscillations at the second oscillation peak
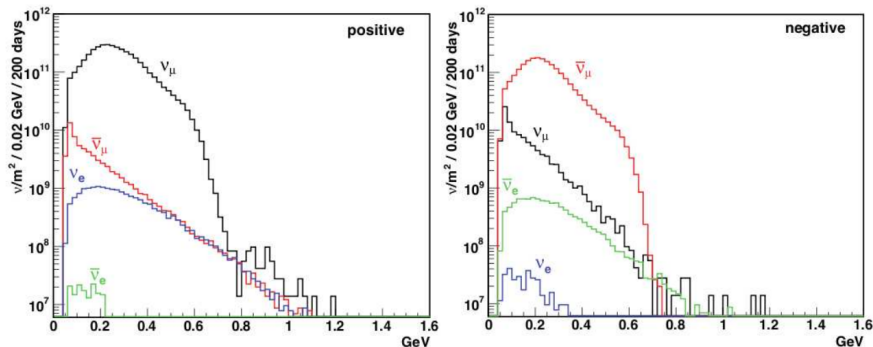
Figure 2.5: Expected neutrino and antineutrino fluxes for positive and negative beams at ESS. From [37].

with a greater resolution and separation from the degeneracy problem we could encounter at the first oscillation peak (see also discussion in section 1.3). Let us discuss briefly the potential of such an experiment in terms of resolution and outreach potential.

Neutrino Super Beam The construction of a neutrino beam line from the ESS Linac would require to double the pulse rate from 14 to 28 MHz, thus doubling the beam power to 10MW to be able to use 5MW only for neutrino production [37]. The high beam power is needed in order to maximize the neutrino flux from the beam and collect the highest possible number of events. Figure 2.5 shows the expected neutrino (on the left) and antineutrino (of the right) fluxes over a 200 days data collection using 2GeV protons. We can see that the result is a high-purity muon (anti-) neutrino beam, with a less than 1% contamination from electron (anti-) neutrino contributions.

Expected performance It is possible to study the impact of systematic uncertainties on the 5σ discovery of δ_{CP} in an Optimistic, Default and Conservative scenario [25]. The table in Figure 2.6 lists those values for each uncertainty source. It is clear that the largest contributions emerge from neutrino fluxes and the cross section determinations. The great power of ESSνSB resides however in the fact that the beam provides a high flux of low-energy high-purity muon neutrinos, below 1GeV. This allows to further reduce the systematic uncertainties since a those energy the main contribution is coming form the Quasi-Elastic (QE) cross section, whereas the Deep Inelastic Scattering (DIS) and Resonance production (RES) provide minimal contributions, as we can see in Figure 2.7. Low-energy neutrinos however require a particular geometry in the detection, since the scattering angles are distributed more homogeneously than in a high-energy beam. This is indeed why the SuperFGD design was chosen for the

Systematics	SB Opt.	SB Def.	SB Cons.
Fiducial volume ND	0.2%	0.5%	1%
Fiducial volume FD (incl. near-far extrap.)	1%	2.5%	5%
Flux error signal ν	5%	7.5%	10%
Flux error background ν	10%	15%	20%
Flux error signal $\bar{\nu}$	10%	15%	20%
Flux error background $\bar{\nu}$	20%	30%	40%
Background uncertainty	5%	7.5%	10%
Cross secs $\times$ eff. QE†	10%	15%	20%
Cross secs $\times$ eff. RES†	10%	15%	20%
Cross secs $\times$ eff. DIS†	5%	7.5%	10%
Effec. ratio ν_e/ν_μ QE*	3.5%	11%	–
Effec. ratio ν_e/ν_μ RES*	2.7%	5.4%	–
Effec. ratio ν_e/ν_μ DIS*	2.5%	5.1%	–
Matter density	1%	2%	5%

Figure 2.6: Systematic uncertainties, respectively optimistic, default, and conservative, for neutrino Super Beams. QE stands for Quasi-Elastic scattering, RES for Resonance production and DIS for Deep Inelastic Scattering. From [25].

ND, as its isotropic geometry provides a good detection efficiency no matter the scattering angle. The fact of having a very precise near detector also allows us to be able to measure for the first time such cross sections with a good precision and further reduce the uncertainties on the models.

It is also interesting to compare the expected discovery potential and resolution of ESSνSB with respect to the two other new-generation long baseline experiments aimed at CP precision measurements, DUNE and Tokai-to-Hyper-Kamiokande (T2HK), the T2K upgrade. Figure 2.8 shows, from left to right, the resolution in the CP angle δ_{CP}, the discovery reach in terms of standard deviations, and the fraction of δ_{CP} values that can be reached with a given significance for the three possible placements of the far detector modules and the comparison with DUNE and T2HK [28]. It emerges that the concept is able to outperform the resolution of the other two experiments, and -optimistically-more than 60% of the δ_{CP} range can be covered. Note that recent results from T2K have constrained the 3σ confidence interval to $[-3.41, -0.03]$ and $[-2.54, -0.32]$ respectively for normal and inverted mass ordering.
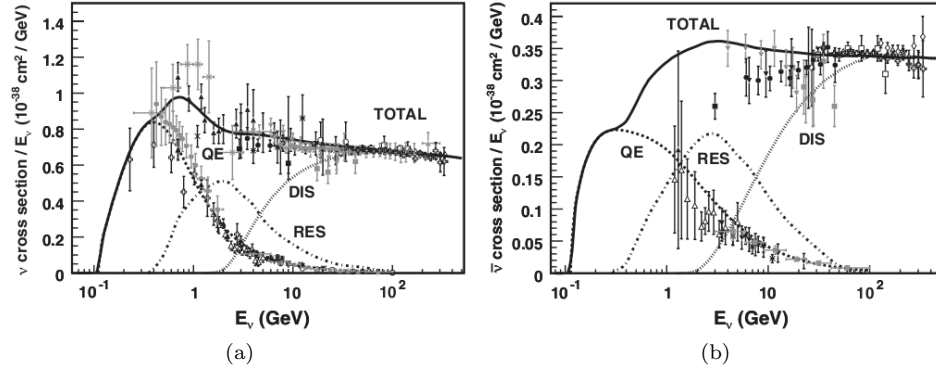
Figure 2.7: Contributions to the total cross section for (a) neutrino and (b) antineutrino scattering interactions.Q E stands for Quasi-Elastic scattering, RES for Resonance production and DIS for Deep Inelastic Scattering. From [30]
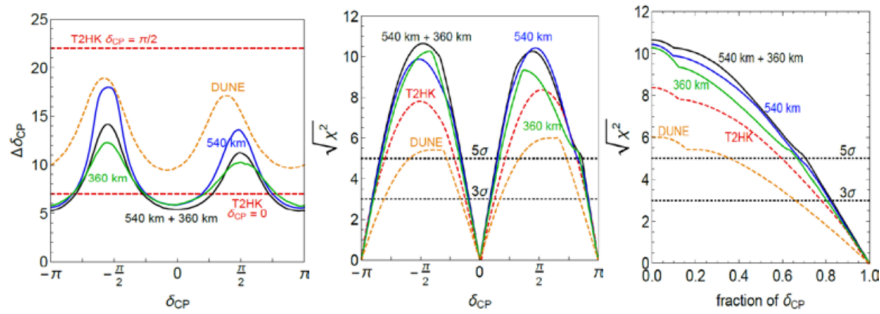

Figure 2.8: Resolution, discovery reach and range fraction covered for the three new-generation long-baseline experiments T2HK, DUNE and ESSνSB. For ESSνSB the three possible far detector locations are considered.

Chapter 3

The Detector

In this chapter we will discuss the physics of particle detectors, with particular focus on the detection techniques useful to understand the working principle of the SuperFGD design. The goal of the first part is to present the behaviour of an organic plastic scintillator when a particle travels through it, by introducing the Bethe Bloch equation that models the energy loss of a particle in a medium and extending the discussion from there. We will mainly follow the concepts presented in the PDG Review *Passage of particles through matter* [63], integrated with some discussions and derivations presented in Leo [41]. Successively we will introduce the SuperFGD design as part of the T2K upgrade of the near detector complex, and describe the experimental setup at CERN used during the collection of the data presented in this study. For this part we will mainly follow the ND280 Technical Design Report [9] and the paper on the first SuperFGD CERN test run (June-July 2018) [7].

3.1   Particle Interactions in Matter

A charged particle moving within a medium can be essentially described considering two effects: the particle losing its energy and its being deflected from its original trajectory. The main contributors to energy loss and trajectory change are primarily from *inelastic scattering with atomic electrons* and *elastic scattering from nuclei*. Other factors include events like bremsstrahlung, radiative losses, or Cherenkov radiation emission. For the latter processes, their occurrence is much rarer when compared to atomic collisions [41]. Inelastic electron scattering is the process that almost exclusively contributes to the energy loss of the incident particle, where the energy is transferred to the atomic electron, which is left excited or even ionized. Note that we should also distinguish between electrons/positrons ($e^{\pm}$) and heavier particles such that their mass $M \gg m_e$. These include muons, pions, and other hadrons.

In this section we will give a description of particles passing through matter, starting from a classical approximation for heavy particles and generalizing it to

include quantum mechanical effects. Furthermore, we extend the discussion to the $e^{\pm}$ case and conclude by introducing the framework of Landau's distribution - a framework better suited when energy loss measurements are required. We will also consider briefly the interaction of neutral photons with the medium.

In general, it is possible to estimate the mean number of collisions with energy loss W in the interval $(W, W + dW)$ in a distance δx from the cross section for the process $\frac{d\sigma}{dW}(W, \beta)$ [63] as

$$\mu_0 = N_e \, \delta x \, \frac{d\sigma}{dW} dW$$

where N_e is the electron density in the medium. Note that for free electrons the Rutherford cross section [64] gives an adequate description. This allows us to introduce a statistical interpretation and define higher-order moments as

$$\mu_k(\beta) := N_e \, \delta x \int W^k \frac{d\sigma}{dW}(W, \beta) dW \tag{3.1}$$

where μ_1 is the mean energy loss, $\mu_2 - \mu_1^2$ its variance and so on.

We will thus be able to define the *stopping power* for a particle in a medium as the average energy loss per unit path length:

$$\left\langle \frac{dE}{dx} \right\rangle \equiv \frac{\mu_1}{\delta x}. \tag{3.2}$$

3.1.1 Classical case

As a preliminary step we should consider the classical limit, which concerns heavy particles where quantum effects can be neglected. The derivation follows closely the one from Born presented in Leo [41], and is useful to get an intuition for the situation we are describing. Let us thus consider a massive particle M with charge Ze passing through a medium with velocity v along the x direction. An electron - assumed to be free and at rest - at transverse distance b is perturbed by the field $E_\perp$ of the incoming particle along the transverse direction (symmetry arguments allow us to ignore other contributions). Note that we assume $M \gg m_e$, therefore the deviation in trajectory can be neglected.

The impulse received by the electron in the collision is

$$I = e \int E_\perp dt = e \int \frac{E_\perp}{v} dx \tag{3.3}$$

and can be estimated using Gauss' Law (in CGS units). We choose as a surface Σ the infinite cylinder with radius b and axis along the x trajectory

$$\int_\Sigma E_\perp d\Sigma = 2\pi b \int_\Sigma E_\perp dx = 4\pi Q_{in} = 4\pi ze.$$

Using the expression for I in equation 3.3 above and using the impulse-momentum theorem $I = \Delta p$, an electron at rest gains an energy

$$\Delta E(b) = \frac{\Delta(p^2)}{2m_e} = \frac{2z^2 e^4}{v^2 b^2 m_e}. \tag{3.4}$$

The energy lost by the incident particle in the volume between b and $b+db$ along the path δx is thus given by all the electronic interactions within the volume:

$$-dE(b) = \Delta E(b) N_e d\tau = \frac{2z^2 e^4}{v^2 b^2 m_e} \, N_e \, 2\pi b \, db \, \delta x = N_e \frac{4\pi z^2 e^4}{m_e v^2} d\big(\log b \big) \, \delta x.$$

The next step consists in integrating out the impact parameter b, but to do so we have to set the integration limits: for $b \to \infty$ the interaction doesn't happen in a short period of time, while when $b \to 0$ we would have infinite energy transfer.

- The maximal energy transfer, considering relativistic corrections, is given by $2\gamma^2 m_e v^2$. If we compare it to equation 3.4, evaluated for $b = b_{min}$, we obtain

$$b_{min} = \frac{z e^2}{\gamma m_e v^2};$$

- In order to obtain an upper limit we need to recall that the electrons are actually bound to atoms. The idea is that we want to avoid adiabatic perturbations, where no energy transfer occurs, by requiring the interaction time (up to relativistic corrections) $\frac{t}{\gamma} = \frac{b}{\gamma v}$ to be shorter than the De Broglie period $1/\nu$ of the bound electron. Thus, considering an average frequency $\bar{\nu}$ over all the bound states, our requirement becomes

$$\frac{b}{\gamma v} \le \frac{1}{\bar{\nu}}, \qquad \text{thus setting the limit} \qquad b_{\max} = \frac{\gamma v}{\bar{\nu}}.$$

Once we consider these extremes and perform the integration, we can get to the result

$$-\frac{dE}{dx} = N_e \frac{4\pi z^2 e^4}{m_e v^2} \log \left(\frac{\gamma^2 v^3 m_e}{\bar{\nu} Z e^2} \right).$$

Again, this expression describes adequately the energy loss for heavy particles, such as α particles or heavier nuclei. When we consider particles such as muons or protons, quantum effects arise and we need to include also those contributions.

3.1.2 Bethe-Bloch equation

The quantum mechanical calculation was first performed by Bethe, Bloch et al. and results in the so-called *Bethe-Bloch equation* [63]:

$$\left\langle -\frac{dE}{dx} \right\rangle = K z^2 \frac{Z}{A} \frac{1}{\beta^2} \left[\frac{1}{2} \log \left(\frac{2 m_e c^2 \beta^2 \gamma^2 W_{\max}}{I^2} \right) - \beta^2 - \frac{\delta(\beta\gamma)}{2} \right] \qquad (3.5)$$

where

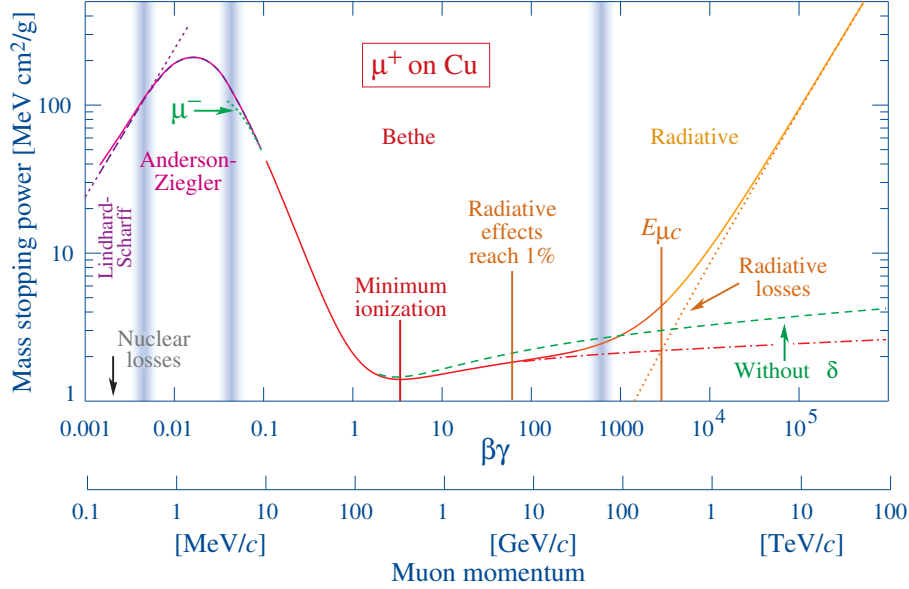- Z and A are the atomic and mass number of the medium;

Figure 3.1: Stopping Power for muons in copper as function of momentum. From [63]

- I is the mean excitation energy for the material [45] (essentially replacing the orbital frequency $\bar{\nu}$);

- $K = 4\pi N_A r_e^2 m_e c^2$ a proportionality factor including Avogadro's number and the classical electron radius;

- $W_{\max} = \frac{2m_e c^2 \beta^2 \gamma^2}{1 + 2\gamma \frac{m_e}{M} + \left(\frac{m_e}{M}\right)^2}$ the maximum energy transfer in a single collision.

Note that this expression gives the stopping power per mass unit; we need to correct it with the material density ρ in order to find the linear stopping power.

The function computed for muons in copper is shown in figure 3.1 and corresponds to the behaviour in the *Bethe-Bloch* region. In this region the only strong dependence is on the relativistic parameter β, taking into account both the maximum possible energy transfer $W_{\max}$ and the flattening of the particle's electric field. The field, instead of causing ionization at larger distances, polarizes the medium, thus limiting the logarithmic increase. This effect is taken into account by the *density effect* term $\delta(\beta\gamma)$, usually computed using Sternheimer's parametrization [62].

The local minimum in the figure corresponds to the minimum ionization of the material and identifies the so-called *minimum ionizing particles* (MIPs): particles that are minimally affected when travelling through the material (since the energy loss rate over travelled distance is minimized).

At higher energies radiative losses become dominant and give the biggest contribution to the stopping power (see paragraph 3.1.3). At low energies, on the other hand ($\beta\gamma < 0.1$), the velocity of the incoming particle is comparable to the electron velocities, and therefore the assumption of free electrons does not hold anymore. Higher-order corrections should then be included in the square brackets of Eq. 3.5:

- When $W_{\max}$ is smaller than the K-shell binding energy, the contribution from these electrons is smaller, and for even lower energies the same happens for electrons in outer shells as well. This effect is taken into account by adding a *shell correction* term $\frac{C_K + C_L + \cdots}{Z}$, which can be found tabulated for common materials [45];

- Qualitatively, the charge of the projectile should influence the electron cloud, which gets attracted by a positively charged particle and gets repelled by a negatively charged one. Thus the stopping power should be slightly smaller for negative beams than for positive ones. That was first noticed by Barkas et al., who noted a difference in range between positive and negative pions [8]. There is no complete theory for this effect, therefore empirical approaches are generally used;

- a correction introduced by Bloch considers the effect of atomic wavefunction perturbations.

PDG's Review of Particle Physics [63] offers an overview of the most commonly used sources for these terms, as well as for the behaviour down to $\beta < 0.05$. For even lower energies, at velocities smaller than the outermost shell electrons, the stopping power scales just proportionally to β [43].

3.1.3 Stopping Power for electrons and positrons

When we consider the stopping power for electrons and positrons, the stopping power is given by the first moment of respectively Møller and Bhabha cross sections [65] from equations 3.1-3.2. The maximum energy transfer is

$$W_{\max} = \frac{1}{2} m_e c^2 (\gamma - 1)$$

where the factor $\frac{1}{2}$ comes from the fact that we are considering identical particles. Thus the logarithmic term is exactly the same as in equation 3.5, to which other effects from kinematics, spin and charge are added:

$$\left\langle \frac{dE}{dx} \right\rangle \propto \log \frac{m_e c^2 \beta^2 \gamma^2 m_e c^2 (\gamma - 1)}{2I^2} + (1 - \beta^2)$$

$$- \frac{2\gamma - 1}{\gamma^2} \log 2 + \frac{1}{8} \left(\frac{\gamma - 1}{\gamma} \right)^2 - \delta \qquad \text{for } e^-$$

$$\left\langle \frac{dE}{dx} \right\rangle \propto \log \frac{m_e c^2 \beta^2 \gamma^2 m_e c^2 \left(\gamma - 1\right)}{2I^2} + 2\log 2$$

$$- \frac{\beta^2}{12}\left(23 + \frac{14}{\gamma + 1} + \frac{10}{(\gamma + 1)^2} + \frac{4}{(\gamma + 1)^3}\right) - \delta \qquad \text{for } e^+.$$

However, this is only a small fraction of the total energy loss. The main contribution comes from ionization processes, while Bremstrahlung becomes dominant at higher energies (ionization energy loss scales logarithmically, while Bremstrahlung is almost linear in energy, see also [63]).

3.1.4 The Landau distribution: most probable energy loss

As pointed out before, the nature of the energy loss through a material is intrinsically statistical. It is therefore possible to obtain the expression for a distribution providing information about the most probable energy loss and its fluctuations in a medium of a given thickness x. The distribution was first derived by Landau [26]. Consider the energy loss by ionization of a *fast particle* through a *thin absorber*. Hence, the energy loss Δ through the material is small compared to the initial energy E_0 of the incoming particle.

The point is to determine the probability distribution function $f(x, \Delta)$ for a particle of given initial energy E_0 losing an amount of energy Δ after travelling through a medium of thickness x. Let us define $w(E, \epsilon)$ as the probability of energy loss ϵ for a particle of energy E per unit length. Our assumption of a thin absorber allows us to remove the energy dependence, as $w(E, \epsilon) = w(E_0 - \Delta, \epsilon) \simeq w(E_0, \epsilon)$. Thus we can write the kinetic equation by equating the rate of change in the distribution function over an interval dx to the *collision integral*, i.e. the difference between the number of particles acquiring the energy E due to ionization losses and the ones leaving the energy level:

$$\frac{\partial}{\partial x} f(x, \Delta) = \int_0^{+\infty} d\epsilon \, w(\epsilon) \big[f(x, \Delta - \epsilon) - f(x, \Delta) \big]. \tag{3.6}$$

The solution can be found by Laplace-transforming the variable Δ, thus defining the Laplace transform of f as

$$\varphi(p, x) \equiv \int_0^{+\infty} d\Delta \, e^{-p\Delta} f(\Delta, x)$$

and its inverse

$$f(x, \Delta) = \frac{1}{2\pi i} \int_{\eta - i\infty}^{\eta + i\infty} dp \, e^{p\Delta} \varphi(p, x).$$

Applying the transformation to both sides of 3.6 leads to

$$\frac{\partial}{\partial x} \varphi(x, p) = -\varphi(x, p) \int_0^{+\infty} d\epsilon \, w(\epsilon)[1 - e^{-p\epsilon}]$$

which allows us to find an expression for $\varphi(x, p)$ having extracted the x-dependence from the integral. To do that, we first have to consider the boundary condition at $x = 0$, for which $f(0, \Delta) = 0$, since at the surface of the medium we require there be only one particle with energy $E = E_0$. This thus leads to the solution

$$\varphi(x, p) = e^{-x \int_0^{+\infty} d\epsilon \, w(\epsilon)[1 - e^{p\epsilon}]}$$

which, once inverted, provides a first solution for equation 3.6:

$$f(x, \Delta) = \frac{1}{2\pi i} \int_{\eta - i\infty}^{\eta + i\infty} dp \, e^{p\Delta - x \int_0^{+\infty} d\epsilon \, w(\epsilon)[1 - e^{p\epsilon}]}. \tag{3.7}$$

Further insights can be obtained if we try to infer the shape of the $w(\epsilon)$ distribution. Consider three characteristic energy values:

- ϵ_0: a typical atomic energy, of the order of mean atomic binding energies;

- $\epsilon_{\max}$: the maximum energy that can be transferred via ionization to an electron;

- ϵ_1: an intermediate value such that $\epsilon_0 \ll \epsilon_1$ and $p\epsilon_1 \gg 1$;

and consider in the integration only those values for which

$$p\epsilon_o \ll 1 \qquad \text{and} \qquad p\epsilon_{\max} \gg 1. \tag{3.8}$$

We can thus split the integral in the exponent of 3.7, which becomes:

$$\int_0^{+\infty} d\epsilon \, w(\epsilon)[1 - e^{p\epsilon}] = p \int_0^{\epsilon_1} d\epsilon \, \epsilon w(\epsilon) + \int_{\epsilon_1}^{+\infty} d\epsilon \, w(\epsilon)[1 - e^{-p\epsilon}]$$

using our definition of ϵ_1 to approximate the first term.

The first term in the integral is just the average energy loss per unit length over the interval $[0, \epsilon_1]$, essentially given by Bethe-Bloch equation 3.5 when considering ϵ_1 as the maximum energy transfer:

$$I_1 := \int_0^{\epsilon_1} d\epsilon \, \epsilon w(\epsilon) = \rho K \frac{z^2}{\beta^2} \frac{Z}{A} \left[\log\left(\frac{2m_e c^2 \beta^2 \gamma^2 \epsilon_1}{I^2} \right) - \beta^2 \right] \equiv \rho K \frac{z^2}{\beta^2} \frac{Z}{A} \log \frac{\epsilon_1}{\epsilon'}$$

where ρ is the medium density.

The second term can be evaluated by identifying the energy loss probability with the formula [26]

$$w(\epsilon) = \rho K \frac{z^2}{\beta^2} \frac{Z}{A} \frac{1}{\epsilon^2},$$

which holds for energy transfers ϵ such that $\epsilon_0 \ll \epsilon \ll \epsilon_{\max}$. Since the integral quickly converges for $p\epsilon \gg 1$ and since we have required $p\epsilon_{\max} \gg 1$, we can extend this relation to the whole integration domain. Inserting this, and after performing a partial integration, we obtain (ignoring for now the overall proportionality constant)

$$I_2 := \int_{\epsilon_1}^{+\infty} \frac{1 - e^{-p\epsilon_1}}{\epsilon^2} = \frac{1}{\epsilon_1} \left[1 - e^{-p\epsilon_1} \right] + p \int_{\epsilon_1}^{+\infty} d\epsilon \, \frac{e^{-p\epsilon}}{\epsilon}.$$

If we then use the approximation $p\epsilon_1 \ll 1$ and introduce the new variable $z \equiv p\epsilon$, the above expression becomes

$$\frac{1}{p} I_2 \simeq 1 + \int_{p\epsilon_1}^{+\infty} dz \, \frac{e^{-z}}{z} \simeq 1 + \int_{p\epsilon_1}^1 \frac{dz}{z} + \int_0^1 dz \, \frac{e^{-z} - 1}{z} + \int_1^{+\infty} dz \, \frac{e^{-z}}{z}.$$

The last two terms above add to give the so-called (negative) Euler-Mascheroni constant $-\Gamma$, thus leading to the result

$$x \int_0^{+\infty} d\epsilon \, w(\epsilon)[1 - e^{p\epsilon}] = x I_1 + x\rho K \frac{z^2}{\beta^2} \frac{Z}{A} I_2 = \xi p \left(1 - \Gamma - \log p\epsilon' \right),$$

where we have defined the new coordinate $\xi := x\rho K \frac{z^2}{\beta^2}\frac{Z}{A}$. We can now use this result in equation 3.7 - and introducing the new variables

$$u := p\xi \qquad \text{and} \qquad \lambda := \frac{\Delta}{\xi} + \log\frac{\xi}{\epsilon'} + \Gamma - 1$$

to simplify the notation - we arrive at an integral representation for our distribution:

$$f(x, \Delta) = \frac{1}{\xi}\frac{1}{2\pi i}\int_{\eta-i\infty}^{\eta+i\infty} du\, e^{u\log u + \lambda u}. \tag{3.9}$$

Considering $u \sim 1$ (a value for which the expression above becomes relevant), we see that the limitations introduced in 3.8 reduce to the conditions

$$\xi \gg \epsilon_0 \qquad \text{and} \qquad \xi \ll \epsilon_{\max}.$$

The first restriction translates into the requirement that the observed energies must be high enough when compared to atomic energies; the second condition is nothing but the initial assumption that the energy loss is small when compared to the initial energy of the incoming particles, as for fast particles (electrons, muons etc.) $E_0 = \epsilon_{\max}$.

A further correction to this result is proposed by Vavilov [66], who introduces a finite limit to the integral in equation 3.6, the maximum energy transfer in a single collision. In both cases the resulting distribution is a highly-skewed curve, the peak of which corresponds to the value predicted by Bethe-Bloch equation 3.5 when we consider also atomic binding corrections. However, the distribution features an important tail towards higher values, that shift the mean to the right and, in experimental situations, is very sensitive to cuts since statistics is generally performed on hundreds of events. Thus the 'mean' in equation 3.5 is ill-defined and it is usually preferred to speak of the *most probable* energy loss, identifying it with the mode of the Landau-Vavilov distribution.

Note that in the case of thick absorbers, the distribution tends to a Gaussian: if we assume that in each collision the energy lost causes a negligible modification in the velocity of the particle, the total energy loss will be a sum of independent contributions each described by a random variable. Thus we are within the hypotheses of validity of the Central Limit Theorem, and the total energy loss is a Gaussian-distributed random variable.

3.2 Scintillators

Scintillators are among the most commonly used materials for particle detection for their quick response time and high versatility. They play a major role in neutrino physics experiments as they can be used both for calorimetric and tracking purposes in near detectors of long baseline experiments with good performance results. The study presented in this thesis is in fact a good example of such devices, as its development arose from the need to improve the detection efficiency of the upstream part of theTt2K Near Detector, which provides good calorimetric measurements but has rather poor tracking resolution.

They rely on the fact that certain compounds release energy in the form of visible light in response to an excitation, which can then be collected with photomultipliers or photodiodes and easily converted into electronic signals. This mechanism is at the foundation of many types of detectors and admit a few interesting features:

- The light yield resulting from a particle scales to a good approximation linearly with the deposited energy. This means that such a device is sensitive to the energy of the particle and can be used as an energy spectrometer.

- The light output coupled with electronics allows for quick response and short recovery time, providing good precision for timing measurements. The short dead times also grant a high count rate and thus a good detection efficiency overall.

- Different kinds of particles trigger different de-excitation (relaxation) mechanisms for some materials, thus providing a way for Particle Identification by analyzing the shape of the measured pulse (Pulse Shape Discrimination - PSD).

If we assume the excitation time to be much faster than the relaxation, we can approximate the light re-emission process as an exponential decay

$$N(t) = \frac{N_0}{\tau_d} e^{-\frac{t}{\tau_d}},$$

where N is the number of emitted photons, N_0 the total number of emitted photons and τ_d the decay constant. This approximation provides a good description of the phenomenon, however more complex decays might be better described by a weighted sum of exponentials with two different decay constants

$$N(t) = A e^{-\frac{t}{\tau_f}} + B e^{-\frac{t}{\tau_s}}.$$

These two components are usually referred to as *fast* and *slow*, and this latter description provides the basis for PSD techniques.

Depending on their relaxation time τ we usually classify scintillation processes into *fluorescence* - with $\tau \sim 10^{-8}$s, of the order of atomic transitions - and *phosphorescence* - with τ on the order of μs to hours. [41].
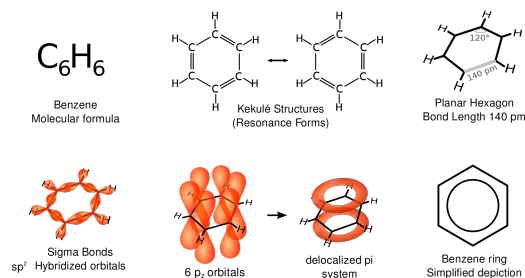
Figure 3.2: Structure of benzene molecule with molecular orbitals. By Vladsinger-Own vector drawing based on layout of en:File:Benzoltrans.png., CC BY-SA 3.0, https://commons.wikimedia.org/w/index.php?curid=7536474

3.2.1 Organic scintillators

Organic scintillators are one of the most common detector materials, due to their plasticity and relatively low cost. The materials used can be plastic, organic crystals, or liquid. Plastic scintillators are by far the most widely used in high-energy physics. However liquid scintillators are becoming more and more common as they easily satisfy large volume requirements. The typical photon yield (luminescence) for a plastic scintillator is around 1 photon per 100eV of deposited energy (see previous section); the resulting signal will then depend on the collection and transport efficiency of optical and electronic systems.

For organic scintillators the light yield is not exactly proportional to the energy deposited, but approaches saturation for higher energy depositions. The radiation in the material generates an exciton (a pair of excited electron and hole) that can then propagate through the material and eventually fluoresces. However in the propagation there are some quenching effects due to the fact that some molecules of the material have been damaged by the incident radiation, and capture the exciton; the probability for this last process to happen is then proportional to the energy deposited. This behaviour has been described by Birks [14], and provides a correction for the luminescence in a scintillator:

$$\frac{d\mathcal{L}}{dx} = \mathcal{L}_0 \frac{\frac{dE}{dx}}{1 + k\frac{dE}{dx}} \tag{3.10}$$

where $\mathcal{L}_0$ is the luminescence at low ionization densities and k an empirical constant, associated to the probability of exciton capture.

The scintillation process in organic materials is associated with the physics of benzene molecular orbitals, present in the compounds. In the ground state, the hybridized sp^2 orbitals form planar $\sigma-$bonds which are completely filled, whereas the six p_z orbitals give rise to off-plane $\pi-$ orbitals, where valence electrons are delocalized. Figure 3.2 shows the structure of the molecule and the ground-state molecular orbitals.
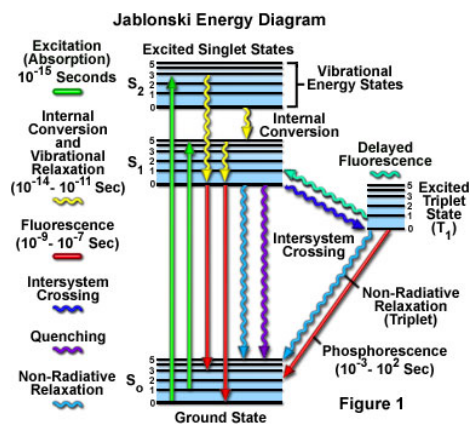
Jablonski Energy Diagram

Figure 3.3: Energy levels diagram of an aromatic compound. From `http://micro.magnet.fsu.edu/primer/techniques/fluorescence/` `fluorescenceintro.html`

The energy levels of the molecule and the relative transitions are illustrated in figure 3.3. Above the singlet ground state S_0 we find the excited singlet states $S_1, S_2, \ldots$ as well as the lowest triplet state T_1 with its excited levels. Each electronic level is also associated with different vibrational modes of the molecule. Usually the excited singlet states decay very rapidly to the S_1 state without radiation emission (internal conversion). From the S_1 level there is high probability for a radiative decay to one of the vibrational states of S_0 ($\tau \sim$ ns). A similar description holds for the triplet states, however the decay $T_1 \rightarrow S_0$ is highly suppressed by spin/parity conservation, thus increasing the lifetime of the state. The main decay mode from T_1 arises through interaction with another excited molecule via $T_1 + T_1 \rightarrow S_1 + S_0 +$ phonons [41, §7.2].

Scintillator materials are complex aromatic compounds, with one or more benzene rings, thus the absorption and emission processes are spread over a wider energy spectrum. Some overlap may also occur, so that a fraction of the emitted radiation is re-absorbed by the material. Because of this, a fluor should have a large enough gap between the major absorption and emission wavelengths (*Stokes' shift*) so that the self absorption is minimized.

The materials used are never pure, but rather solutions made of an aromatic compound as a base where one or two fluors are dissolved. This happens basically for two reasons:

i. Quenching effects and self-absorption of the radiation may occur, and this shortens the attenuation length of the material (i.e. the distance after which the probability for the propagating particle to not be absorbed has dropped by $1/e$, as it scales exponentially according to Beer-Lambert law [63]). The dissolved fluor here acts as a *waveshifter*, absorbing the radiation and re-emitting it at wavelengths the base is more transparent to, thus increasing the attenuation length.
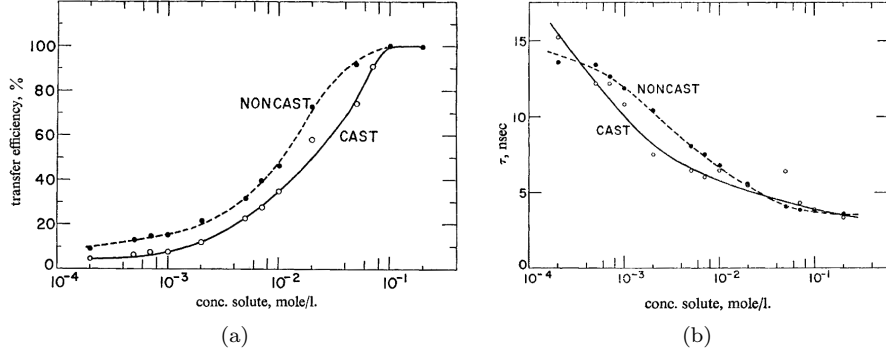
Figure 3.4: Efficiency q (a) and decay time τ (b) for radiative processes as function of primary fluor concentration. From [11].

ii. For radiative processes, the decay times τ_r can be rather long and the efficiency q_r quite low. If we consider for instance polystyrene, the radiative and non-radiative rates are respectively [42]:

$$k_r = 1.98 \times 10^6 \text{s}^{-1}; \qquad k_{nr} = 5.02 \times 10^7 \text{s}^{-1}$$

translating into a decay time of

$$\tau_r := \frac{1}{k_r} = 500\text{ns}$$

with an efficiency of

$$q_r := \frac{k_r}{k_r + k_{nr}} = 3.8\%.$$

The addition of another organic scintillator (at concentrations $\gtrsim 1\%$ in volume) as primary fluor causes a non-radiative resonant dipole-dipole coupling that contributes to the energy transfer, shortening the decay time and sharply increasing the efficiency of the radiative processes - and thus the light yield. Figure 3.4, taken from [11], illustrate how efficiencies and decay times vary for different concentrations of p-terphenyl in a polystyrene base: it is possible to get to an almost 100% efficiency and decrease the decay times down to 2ns.

The collection of photons is aided by the use of external *wavelength shifters*, especially when the geometry of the system becomes more complex: the light is captured in a pipe made of a solution of wave-shifting fluor in a non-scintillating base, that transports the light signal to the electronics which then processes it.

3.3 T2K ND280 and SuperFGD

The prototype detector considered in this thesis is inserted in the context of the upgrade of ND280 of the T2K experiment [3], the Near Detector shown in figure 3.5 and located 280m downstream from the beam source. The upgrade is needed in order to match the program for T2K phase II of constraining CP violation measurements down to 3σ precision and reduce systematic uncertainties from $\sim 6\%$ to $\sim 4\%$ [16]. The main reason for this improvement comes from the upgrade of the active scintillator target to a high-granularity device using the Super Fine-Grained Detector (SuperFGD) design, i.e. a matrix of 1cm side scintillator cubes each read out by three Wavelength shifting (WLS) fibers. This section focuses on the detector setup, design and tests performed with a SFGD prototype detector at CERN.
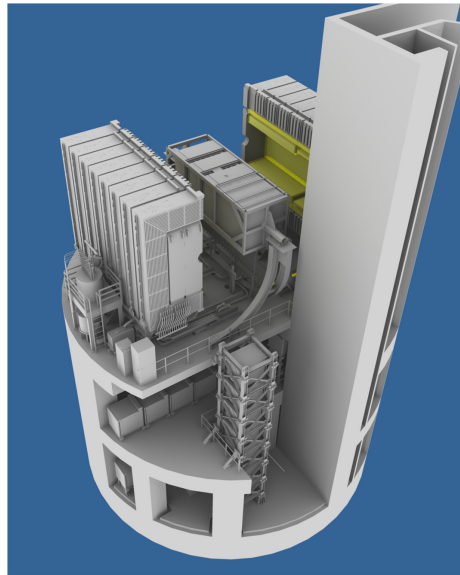
Figure 3.5: Render of the near detector ND280 of the T2K experiment, in the underground pit setup. From [3]

3.3.1 ND280 Setup and Upgrade

Figure 3.6 shows schematically the setup of the detection system for the near detector of T2K. A proton beam hitting a graphite target produces a pion and muon beam that enters the system from the right. The initial setup consists in the upstream part of a thin Electromagnetic Calorimeter (ECal), made of alternating layers of lead and plastic scintillator bars, followed by the π_0 detector and another thin ECal. The downstream part consists of alternating Time Projection Chambers (TPCs) providing information about momenta of charged
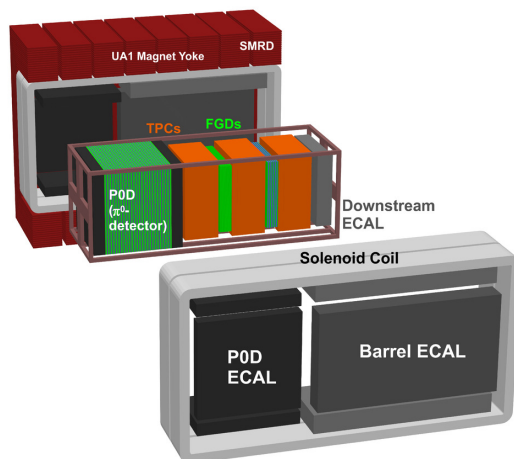
Figure 3.6: Representation of the current ND280 detection system.

particles as well as Particle Identification (PID) through dE/dx measurements to two scintillator Fine-Grained Detectors (FGDs). The first one consists in stacked layers of polystyrene orthogonal to the beam, forming the active mass for neutrino interactions as well as providing tracking information. The second one alternates layers of plastic material to layers of thick water, providing information about the ratio between the interaction cross section in carbon and water when combined with the data from the first FGD[3]. The whole core detector is inserted in a magnetic field, essential to determine charge and momentum information, and surrounded by electromagnetic calorimeters which further improve PID allowing to efficiently discriminate between muons and electrons.

Such setup has its main strength in allowing momentum and charge determination for the pions, thus making it possible to distinguish between neutrinos and antineutrinos and providing effective PID information. A pion $\pi^{\pm}(\overline{[d]}u/\overline{[u]}d)$ for instance decays in $\sim 99.9\%$ of cases [63] via the weak process

$$\pi^- \to \bar{\nu}_\mu \mu^-$$
$$\pi^+ \to \nu_\mu \mu^+$$

by the conversion of a $W^\pm$ boson into a lepton-antilepton pair. Now, charge conservation implies that if the pion is negatively charged, then the charge of the lepton-neutrino pair is negative too, thus the process results in the production of a negatively charged lepton and an antineutrino. The same argument holds if we consider the charge-conjugated process, and thus a positive pion will decay in a neutrino-antilepton pair.

However, most of the events are selected by looking at the interactions in the downstream FGDs and the subsequent TPC: this gives a great efficiency in the forward region for transverse angles $\theta < 40°$ with respect to the beam
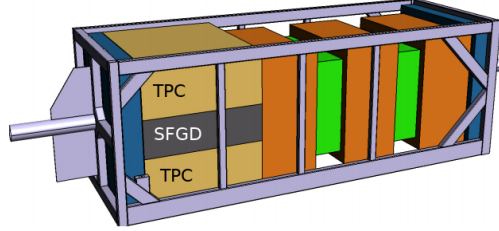
Figure 3.7: Sketch of the upgraded ND280 detector, with the SuperFGD SD and the High-Angle TPCs. Beam enters from the left side.

axis, but the efficiency drops abruptly for scattering angles outside this cone. Furthermore, at energies below 1GeV the muon/electron tagging is not effective as the tracking information is poor and gamma conversion processes add extra noise. This factor introduces a non-negligible systematic uncertainty in the determination of ν_e/ν_μ cross section ratio and flux and limits the capabilities of the detection system, even with larger statistics. Thus, an upgrade to ND280 [16] was needed in order to

- track muons produced in charged-current interactions with full and precise polar angle acceptance, without losing energy and momentum resolution;

- have a full 4π tracking efficiency for low energy pions and protons, to determine the event topology and have a good pion-proton identification;

- obtain a good timing information for the tracks entering the TPCs, thus contributing to the PID.

The upgrade concerns the upstream part of the detector (P0D), which is to be replaced by a high granularity scintillator detector (SD) using the SuperFGD design between two horizontal High-Angle TPCs, as displayed in figure 3.7. The downstream system is left essentially unchanged. This way charged particles produced in the SD area are detected directly inside the detector, thus granting an almost full polar angle coverage.

In this context we will focus on the scintillator detector, as the analysis presented later in this thesis aims to test the features of a prototype detector for such system.

3.3.2 SuperFGD Scintillator Tracker

The SuperFGD design consists of a 3D array of $1 \times 1 \times 1\text{cm}^3$ size optically independent scintillator cubes, where the light signal is read out by three orthogonal WLS fibers. Each cube has three holes, corresponding to the x, y, z axes, where the fibers are inserted. The signal from the fiber is then read by a Multi-Pixel Photon Counter attached to one end of the WLS. This system allows to get
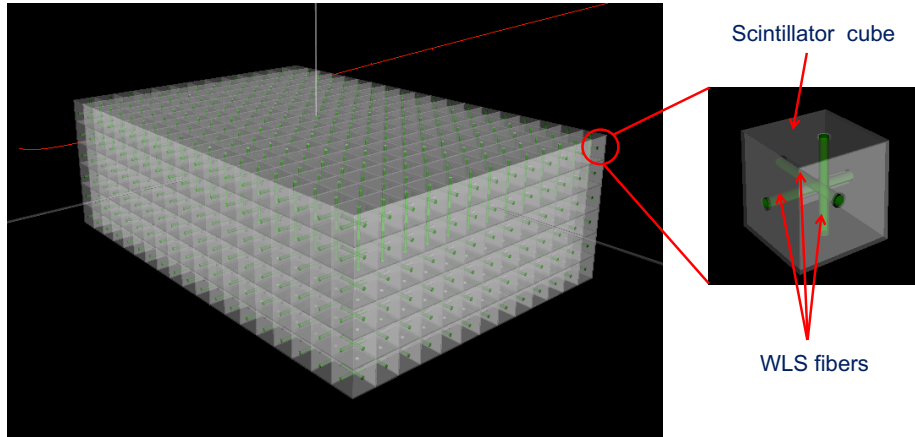
Figure 3.8: Scheme of the SuperFGD tracker structure, with close-up on a cube with WLS readouts.[9]

projections of charged particles onto three planes without inactive regions, and provides a much larger amount of information about neutrino interactions with respect to the previous system. Figure 3.8 shows the structure of the cubes array forming the Scintillator Tracker, with the orthogonal WLS fibers.

Cubes and WLS fibers The scintillator cubes are made of a base of polystyrene, with 1.5% paraterphenyl (PTP) as primary fluor and POPOP (0.01%) as secondary fluor, matching the absorption peak of the WLS fibers. The optical isolation is induced by treating the cube faces with a chemical agent, which forms a white polystyrene micropore deposit resulting in a $50 - 80\mu m$ thick reflective layer. Three orthogonal holes of 1.5 cm diameter are drilled to insert the WLS fibers. The fibers themselves are the same used in the current ND280, namely multi-cladded round fibers with $1.0mm$ diameter, with absorption peak at $\lambda = 430nm$. Table 3.1 summarizes the main features of the WLS.

Photosensor To detect scintillation light the Multi-Pixel Photon Counter (MPPC) from Hamamatsu Photonics K.K. is used, as it has been successfully for all scintillation detectors of T2K since 2009 [3]. It has a sensitive area of $1.3 \times 1.3mm^2$ as for the current ND280, and it is designed to match the WLS fiber diameter. The pixel pitch has been decreased form 50 to $25\mu m$ (i.e. increased the pixel density) in order to get a larger dynamic range, reducing the dark and readout noise. Furthermore, thanks to the continuous developement since the original model, dark noise rate, cross-talk probability and afterpulse probability have dropped by about an order of magnitude [9, §2.4].

Electronics The basic design for electronic readout borrows the one used for the Baby MIND collaboration, namely the CITIROC readout chip [48].

Item	Specification
Fiber type	Round shape, Multi-cladding
Diameter	1.0 mm
Materials	Core: Polystyrene (PS),
	Middle clad: Polymethylmethacrylate (PMMA),
	Outer clad: Fluorinated polymer (FP)
Refractive index	Core: 1.59, Middle clad: 1.49, Outer clad: 1.42
Density	Core: 1.05 g/cm^2, Middle clad: 1.19 g/cm^2,
	Outer clad: 1.43 g/cm^2
Absorption wavelength	430 nm (peak)
Emission wavelength	476 nm (peak)
Trapping efficiency	∼5.4%
Attenuation length	>3.5 m

Table 3.1: Main specifications of the WLS fiber, Y-11 (200) by KURARAY Co. Ltd. From [9].

The core of the electronics is a Front End Board (FEB) hosting 4 CITIROC chips with 32 channels each connected to the MPPCs, an Analog-to-Digital (ADC) converter and a Field-Programmable Gate Array to manage data flow and timing information. A more detailed scheme of the FEB architecture is shown in figure 3.9. In order to get the largest possible dynamic range, the CITIROC can be set in two different pre-amplifier paths, a High Gain and a Low Gain one, thus being able to reach a signal resolution from 1 to 2000 photoelectrons with a 10:1 signal-to-noise ratio.
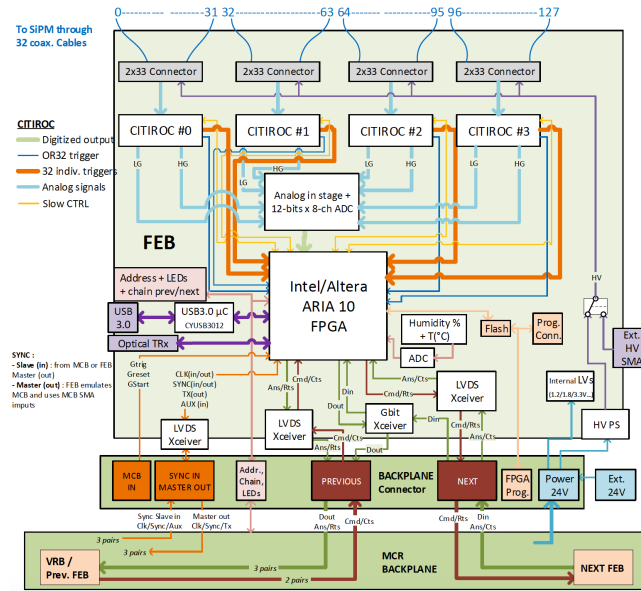
Figure 3.9: Scheme of the FEB architecture. From [9]

3.4 The prototype

This thesis focuses on the analysis of the data set collected during the test run for a $24 \times 48 \times 8$ cubes prototype detector, assembled to assess the features and performances of the system before the construction of the detector itself. This section presents the specifications of the prototype, as well as a description of the experimental setup during the second test beam run, hold in August-September 2018 at CERN, with a mixed proton, pion and lepton beam.

3.4.1 Prototype

The prototype is composed of 8 planes of 24×48 cubes, stacked over each other and separated by reflective layers of Tyvek paper (only for developement purposes, not considered in the final design). The WLS fibers are equipped with three different types of photosensors, of which the majority are the Multi-Pixel Photon Counters (MPPCs) chosen for the ND280 upgrade (S13360 - *Type I*), but two other types are used as comparison (S13081 - *Type III* and S12571 - *Type II* respectively, from the beam entry point). Figure 3.10 shows the distribution of the different photosensors on the detector. The detector is equipped with the electronics developed for Baby-MIND, i.e. based on the CITIROC design, since it was chosen as the basis for the actual SuperFGD design. The dimensions have been chosen in order to fit the MNP17 magnet of CERN T9 beam line, the facility chosen for the test run. Figure 3.11 shows the prototype without electronics before the insertion in the beam line.

The signal readout follows three different paths, providing a measurement of amplitude [9, §2]:

i. HG path, calibrated by calculating the ADC-per-photoelectron (PE) gain ratio for each channel from a known signal (LED or dark counts -event counts arising from dark currents in the material and not optical processes)

ii. LG path, calibrated by comparing LG and HG data for the same events and the same channel

iii. a Time over Threshold (ToT) measurement, sampling the rising and falling edges of the CITIROC trigger lines; the calibration compares ToT data and HG data (up to 100 PE) or LG data (over 100 PE).
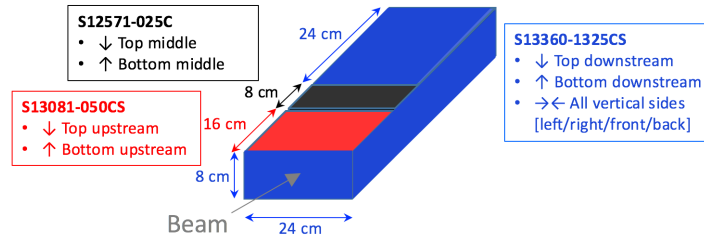
Figure 3.10: Distribution of the three different photosensors around the detector mass. S13360-1325CS is the one chosen for the upgrade.
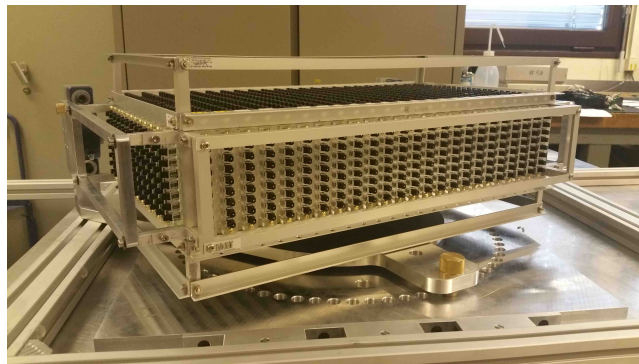
Figure 3.11: Photo of the assembles SuperFGD prototype, with WLS fibers and optical connections.

3.4.2 Experimental setup at CERN T9 beamline

The prototype was shipped to CERN in May 2018, and equipped with electronics before it was installed in the T9 beam line ready for the test runs. Two different runs allowed data collection, the first one during June-July, without TPC. Time of Flight counters provided the information on particle identification. The August-September test phase had also the TPC on the beam line. Figure 3.12 shows the layout of the experimental setup and beam line components.
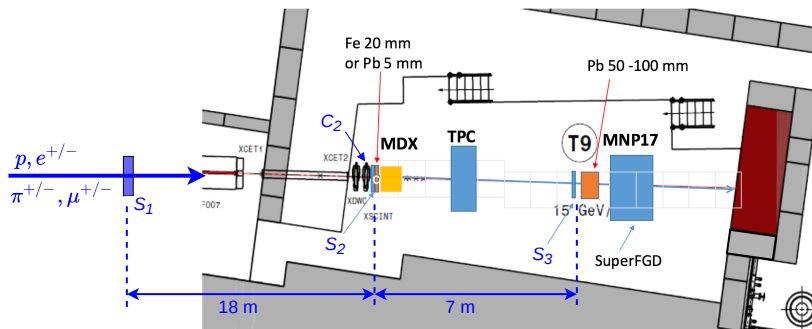

Figure 3.12: Layout of T9 beam line components during the test runs.

The protons colliding in the North Target of the CERN East Area [27] generate a mixed hadron and lepton beam that can be discriminated into positive and negative charge before it is injected into the T9 beam line. The beam momentum can also be controlled through a system of magnets, and was fixed for each experimental run. Two main beam modes were operated [7]:

- *hadrons*, with a mix of protons, pions, electrons and muons, whose relative fraction could be modified using beam stoppers and converters;

- *muons*, with a thicker beam stopper to suppress hadronic and most of electronic contributions.

The beam successively travels to the TPC and SuperFGD target, where particles are detected. The MDX magnet is operated at 1.0T only for photon data collection, where only neutral particles are selected. The MPP17 magnet is operated at 0T, 0.2T and 0.7T. A thicker Pb target is placed before the scintillator target to collect stopping muon data. The data sets include also cosmic data, acquired without incoming beam and using trigger information from surrounding detectors [9].

The data acquisition for the beam test runs is controlled by the trigger information from three scintillator detectors $S1, S2, S3$ and a Cherenkhov detector C_1, used for particle identification. This information is used as trigger for data acquisition, storing only events with the desired particle species: $p, e^{\pm}, \mu^{\pm}, \pi$ [7].

Further details about the data set itself will be given in the following chapter, where we will consider the analysis of the data collected during the second

test run at CERN (August-September 2018) in terms of response to Minimum Ionizing Particles.

Chapter 4

SFGD test beam data analysis

This chapter is focused on presenting the study in terms of energy response to Minimum Ionizing Particles (MIPs) of the data from the second test run of the SuperFGD prototype at CERN. We will first shortly describe the dataset and show some type of events that are included, and present some preliminary considerations about the detector behaviour and data selection. Successively we will consider the detector response to a MIP by isolating the signal and using it to test the performances of the detector readout channels. A tentative study of the effect of magnetic bending to the light yield is then presented, motivated by the measurement of 3% increase in photoelectron emission for a plastic scintillator in a 0.45T magnetic field [13, 63].

4.1   Dataset

The dataset we consider in this analysis is what has been collected during the experimental run at CERN in the period August-September 2018. Two beam modes were operated: *hadrons*, with mixed $p, e^{\pm}, \mu^{\pm}$ and $\pi^{\pm}$ signals, and *muons*, with muon signals and $10-20\%$ electron contamination [7]. The magnet system at the beginning of the beamline allows to select particles depending on their charge and momentum, thus collecting events in the range $[\,0.5\,,\,8\,]\mathrm{GeV}/c$ for both positively- and negatively-charged beams. The other varying parameter is the magnitude of the MNP17 magnetic field presented in the previous chapter, set to a value chosen between 0T, 0.2T and 0.7T. The particular configurations are summed up in Table 4.1.

The raw data from the Font-End Boards (FEBs) has been processed into a hit- and event-based format analogous to the babyMIND data processing [48] in order to simplify the handling of the datasets. This means that the FEB information is assembled into a set of events, each containing a number of hits,

beam mode	**B**[T]	(charge)**p** [GeV/c]
hadrons	0	0.8,-4,-5,-8
	0.2	0.5,-0.8,1.0,2.0
	0.7	1.0, 0.5
muons	0	0.5
	0.2	0.5,2.0
	0.7	2.0

Table 4.1: Momentum and magnetic field configurations in the dataset for the two main beam modes.

corresponding to every time each fiber detects some signal. The further analysis is performed using the CERN ROOT [18] libraries embedded in a set of C++ functions.

4.1.1 Track visualizations

The first thing we can extract from the data is the visualization of the tracks for each event by considering the number of Photoelectrons (PE) collected from each fiber. Some visualizations are presented in Figure 4.1, where we can see the energy (PE) deposited in each fiber across the cubes; namely the XY-view shows the energy deposited in the fibers parallel to the z-axis and the beam direction, the ZX-view would be the top of the detector, while the ZY-view is the side view.

First we can notice that there are some events, like the one shown in Figure 4.1a, where the triggers are activated but no tracks are detected. Those "fake" events result in a multiplicity of low-energy hits that might introduce a source of noise. A first way to discriminate it is discussed in the next section; however, such hits are found as background noise also in events where tracks are registered, and thus more difficult to be filtered out completely. These events are concentrated at the beginning of each dataset, therefore we introduce a selection to reject the first 50 events of each file, to reduce the molteplicity of those tracks.

Two interesting events are the ones shown in Figures 4.1b-c, coming from the 0.5G/c beam in hadron mode. Here we see a charged pion decaying into a muon and a muon neutrino -the latter leaving no track in the detector. In the event of Figure 4.1c the neutrino interacts via weak interaction with the detector material leading to a charged lepton, whereas in Figure 4.1b the neutrino travels outside the detector, making this event the ideal candidate for neutrino oscillations experiments. Such processes are in fact the simplest source for a neutrino beam: once a pion decay is detected and its charge determined, it is possible to select the momentum of the produced neutrino such that its trajectory is directed towards a far detector where it can be detected if it interacts with the detector volume.

Another significant track example is shown in figure 4.1d, from a $0.5\mathrm{GeV}/c$ event still in hadron beam mode. This is an example of photon conversion, where an incoming photon (unbent in the magnetic field) decays into an electron-positron pair, with opposite bending due to the opposite charge. A second photon, expected in the process because of energy conservation, is absorbed by the material close to the branching point where we have high PE deposition, and thus does not form any track.

One last visualization from the hadron beam mode is presented in figure 4.2. The tracks shown in the top figure have a well defined and contained distribution in the XY plane, with a homogeneous energy loss until the point where we see a peak in the energy deposition (bottom figure). This corresponds to a stopping proton, which propagates in a straight line (slightly bent in the ZX direction because of the 0.7T magnetic field) until it stops, depositing all the remaining energy in a limited area. This feature is underlined in the energy deposited along the z-coordinate, where we can clearly distinguish a Bragg Peak in presence of the stopping point in the right plot of Figure 4.2b.

The tracks we will consider in this analysis are obtained from the other beam mode -muons- and will be discussed in the next section.

4.2   Preliminary considerations on detector response

As a first visualization, we consider the full data set of the *muon* beam mode, since it provides only clean μ^- events with a minor e^- contamination. A typical event is shown in figure **??**. Note that the PE scale of the XY view is about a factor 10 higher than the other two views, since the long longitudinal fibers collect photoelectrons from multiple hits stacked with the same coordinates and thus become saturated. The hits are in fact acquired within a specified time frame from the trigger, and the longitudinal fibers collect all the PEs emitted in the cubes throughout the whole detector length within the time acquisition frame. Therefore, for the further energy studies we will only consider the top and side view. Furthermore, to reduce the noise coming from events like Figure 4.1a we reject the first 50 events from the start of the acquisition, as well as the events with less than 50 hits in the detector. This brings the number of total events considered from 1544945 to 1263149.

We are interested in the light yield, or number of photoelectrons (PE) deposited by each hit in a fiber, as it can be related to the energy deposition by simply inverting equation 3.10. Figure 4.4a shows a bimodal distribution, with two distinct peaks:

- the first one is for low-energy hits, and are analogous to the peaks with average charge of 4.5 PE corresponding to the secondary peaks from the hit-from-trigger distribution observed in [7], whose origin is not well understood. The same reference performs further analyses by adequately
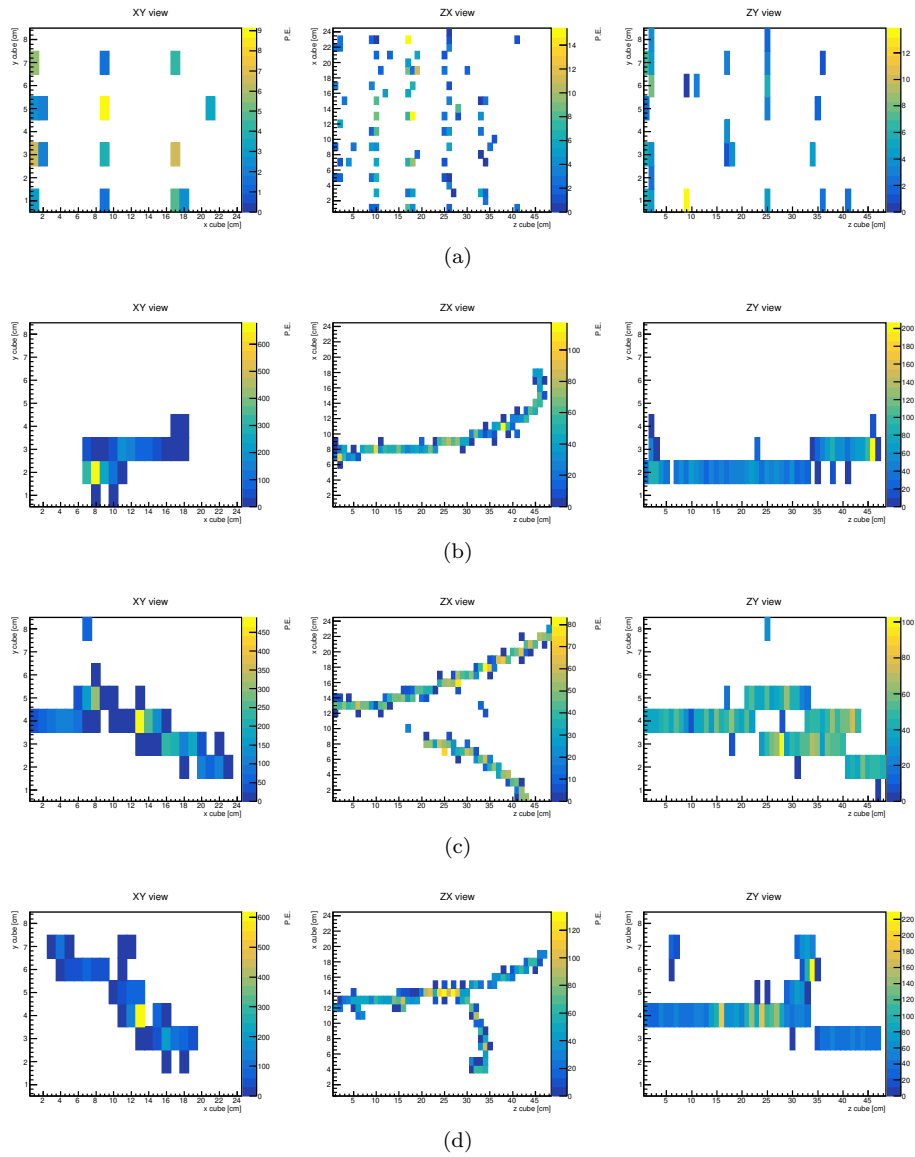
Figure 4.1: Example of track visualizations obtained from the dataset. The front, top and side views are presented from left to right.
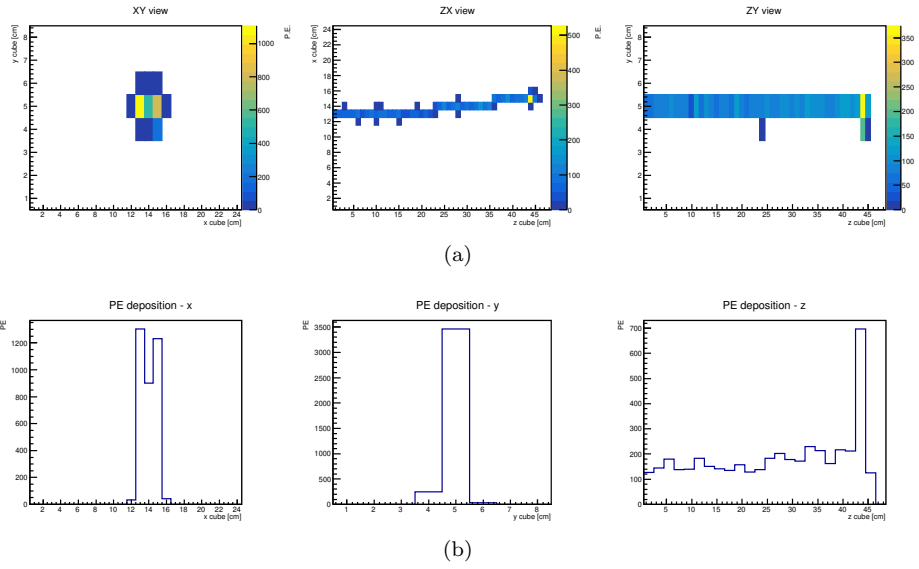
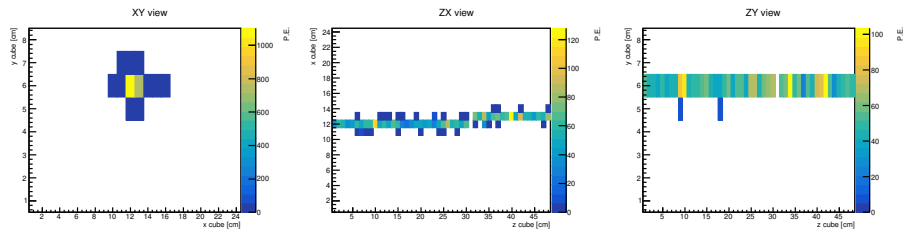Figure 4.2: Tracks and PE per fiber from a proton stopping inside the detector volume.

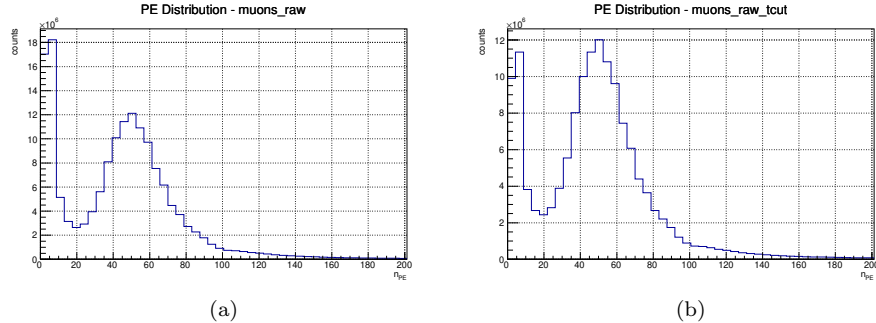Figure 4.3: Front, top and side tracks from a muon traveling across the detector area.

Figure 4.4: PE per fiber deposited in the detector for the raw dataset (a) and after the timing cut (b).

	n. events
Before Δt cut	1263149
After Δt cut	1239821

Table 4.2: muon mode dataset size before and after the Δt selection.

selecting the time window to minimize the contribution of those peaks.

- the second peak, around 50 PE, is the one associated to the minimum-ionizing particles (MIPs) energy deposition, and reflects the behaviour of muons passing through the medium, where their energy loss is minimal and thus almost constant along the z-coordinate (this essentially corresponds to the minimum of the curve shown in figure 3.1).

If we focus on the first peak and try to filter it out, we should consider the distribution of the hit time from the trigger, set at -250ns. Figure 4.5 shows this distribution for both the whole dataset and the low deposition hits, with less than 10 PE deposited. We see that for more than 145ns from the trigger time ($\Delta t > -105$) the contribution of those hits is still significant if not dominant.

If we then introduce a cut and suppress all the events with $\Delta t > -105$ns, we obtain the distribution of figure 4.4b, where the low-PE peak is still present, yet not dominant, and we haven't lost a significant number of events nor resolution for the MIP peak. Table 4.2 shows the size of the dataset before and after the Δt cut is implemented. $\sim 2\%$ of the initial dataset is rejected.

4.3   Response to Minimum-Ionizing Particles

In order to study the response of the detector to minimum ionizing particles, we should introduce some basic selections to the dataset we are considering.
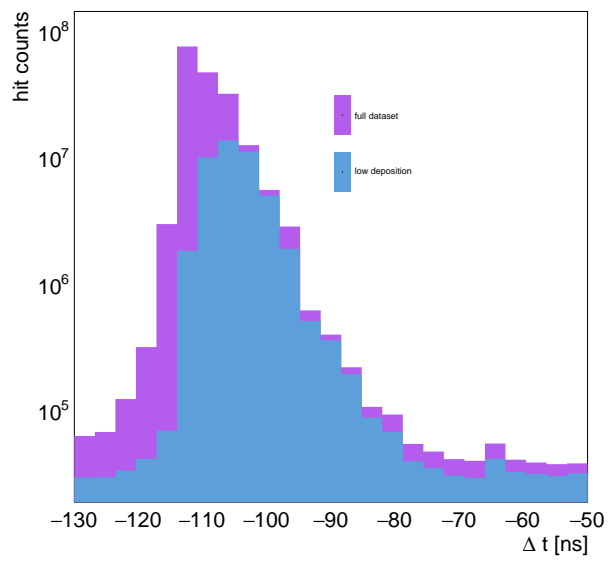
Figure 4.5: Time from trigger distribution for hits in the muon beam mode. Distribution for low-energy ($< 10PE$) hits only is also displayed.

This allows us to remove most of the noise introduced by bad data acquisition and to filter out events that would affect the shape of the distribution we want to consider, such as particles stopping inside the detector or decaying into subproducts. Specifically, the selections we introduce are the following:

- *Maximum energy deposited.* We require the particle passing through to be a MIP, rejecting any events with more than 100 PE deposited in one fiber.

- *No Gaps.* We require the track left by the particle to be ideally continuous, by rejecting events that do not show energy deposition in three or more consecutive detector layers. This allows us to filter out some of the malfunctions in the MPPC photon counters.

- *Containment.* We require the trajectory of the particle to be confined within the detector mass in the X and Y directions, by rejecting all events showing hits in the outer layers.

- *Non-stopping.* We require the particle to actually pass through the detector and get out, by rejecting all the events with no hits in the fibers with z-coordinate at the end of the detector (z=48).

- *y-Confinement.* We require the energy deposition along the y-coordinate to be mostly confined within a single cube by rejecting all events with a standard deviation bigger than 1.0 in the PE distribution in the y-direction. This allows us to reject most of the events where the particle decays and the track starts branching.

This, together with the initial selections on hits and time from trigger, allows us to select 1015618 of the total 1544945 events, corresponding to $\sim 66\%$ of the initial dataset.

4.3.1 Channel Uniformity

We want to analyze the response of each fiber connected to a MPPC channel and point out potential differences. In order to do so, we consider the PE distribution for each single fiber and try to extract the most important features. The objective is identifying the MIP peak for each readout and analyze its distribution and properties. We therefore perform a gaussian fit in the interval $[20\,,\,150]$PE for each of these distributions to exclude the low-energy peak. The fit is then performed if the hit entries are at least 150. Below that value we cannot perform a proper measurement, since the low-energy peaks become too relevant and there are not enough hits to be able to resolve different distribution shapes.

Figures 4.6 and 4.7 show some of those distributions for the fibers in the two transverse directions to the beam axis (z-coordinate), together with the gaussian curve fitted to identify the peak. The first evident feature is that we

have more definite peaks close to the axis of the detector ($x = 12, y = 8$), since we have deliberately selected tracks that run through the whole detector area without decaying or abruptly changing trajectory. The peaks are also higher for extremal $x-$ coordinates towards the end of the detector as here the bending effect of the magnetic field causes a bigger spread from the distribution at the entrance point $z = 1$.

Another feature is the difference in the readout distribution due to the different MPPCs used through the detector volume, as shown in figure 3.10. In particular it is possible to distinguish clearly the distributions from Type II MP-PCs in the vertical (z,x) fibers for $x \in \left[17\,,\,24\right]$, where the main component of the signal comes from a time-over-threshold (ToT) measurement and the peaks are discretized. This provides a source of uncertainty when fitting for a MIP peak, since the irregularity in the distributions not always allows to clearly distinguish this shape, and for low number of hits it shifts the peak towards low PE values.

Due to the reduced volume and to the beam shape along the y-coordinate that provides more hits for the same fiber -and therefore more statistics- the distributions for the transverse horizontal (z,x) fibers are more regular and defined, and -away from the detector edges- they all show a MIP peak around the value of 50 PE. Furthermore, the events are all acquired with the same kind of MPPCs (Type I), thus eliminating further noise and fluctuations coming from the different electronics.

At this point it is instructive to plot the results of the gaussian fits for the PE distribution of each single fiber to see how it behaves with respect to the others and spot eventual malfunctions in the MPPCs. Figure 4.8a-c shows an example of these visualizations for three different (z,x) and (z,y) combinations. The uncertainty shown corresponds to the 1σ interval around the fitted mean. All of those plots show a mean value oscillating around ~ 50 PE. However, there are some isolated points who stand out and might suggest that something has gone wrong either in the data acquisition electronics or in the fitting procedure. In Figure 4.8a for instance, the $z = 28$, $x = 9$ shows a much higher mean value -around ~ 80 PE. This value comes from the fit on the distribution in figure 4.9a, where the peak is shifted towards higher PE values. Another point that stands out is for the $z = 37$, $y = 6$ fiber, that comes from the fit of distribution in Figure 4.9b. Here there is a single peak, that merges the MIP and low-energy peak signals. Both this and the former deviations can be explained in terms of a malfunction in the data acquisition, probably due to a defective MPPC or WLS fiber.

Last, if we consider Figure 4.8c we see a set of points in the interval $z \in [17, 24]$ where the value registered in the x-coordinate is much lower than the others. These come from the fit on distributions like Figure 4.9c, where the alternate height of the peaks coming from low ToT resolution cannot allow the fitter to resolve the MIP peak, that merges with the end of the low-energy peak, shifting the average towards lower values.

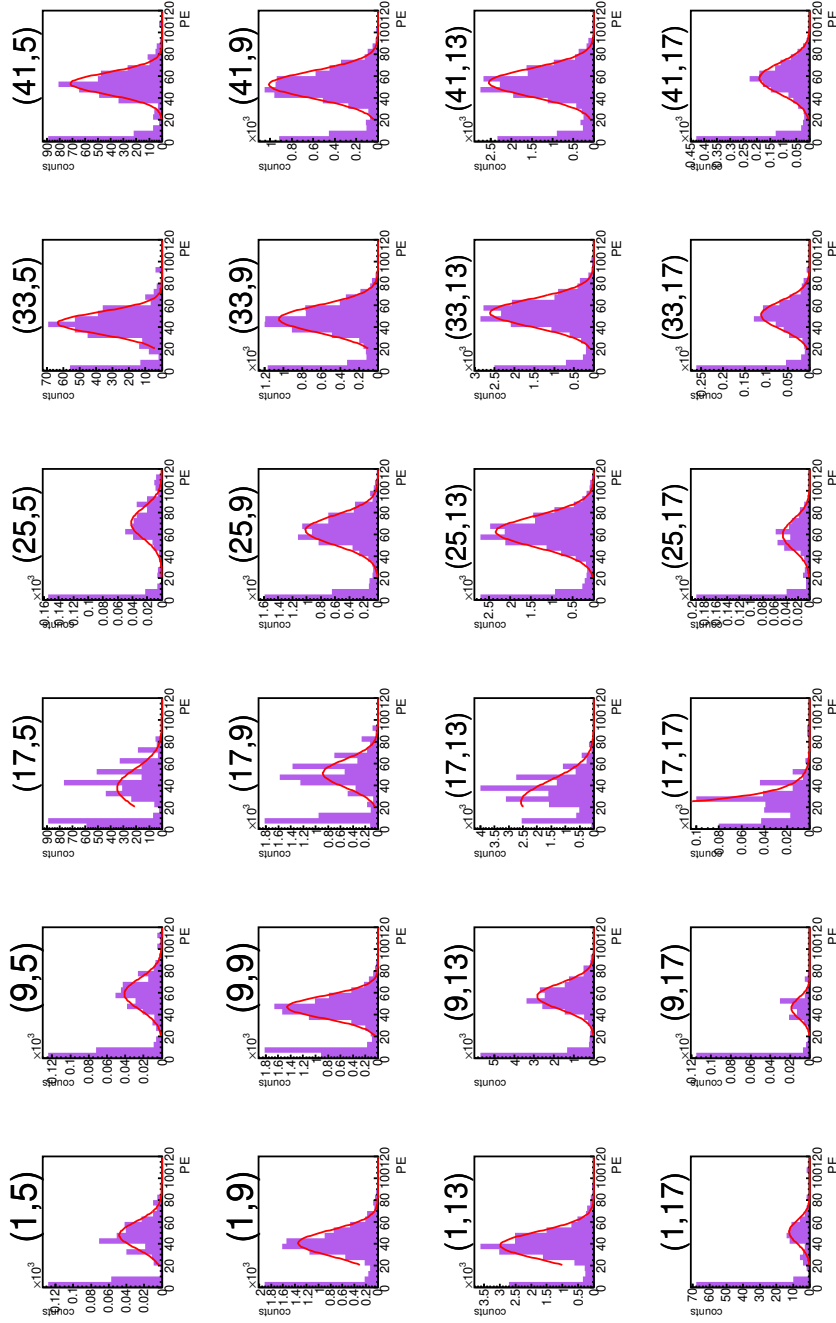This underestimation of the mean in the Type-II MPPCs is even clearer if we

Figure 4.6: PE distribution per fiber in the (z,x) direction for MIPs. The red curve corresponds to the gaussian fitted for each fiber.
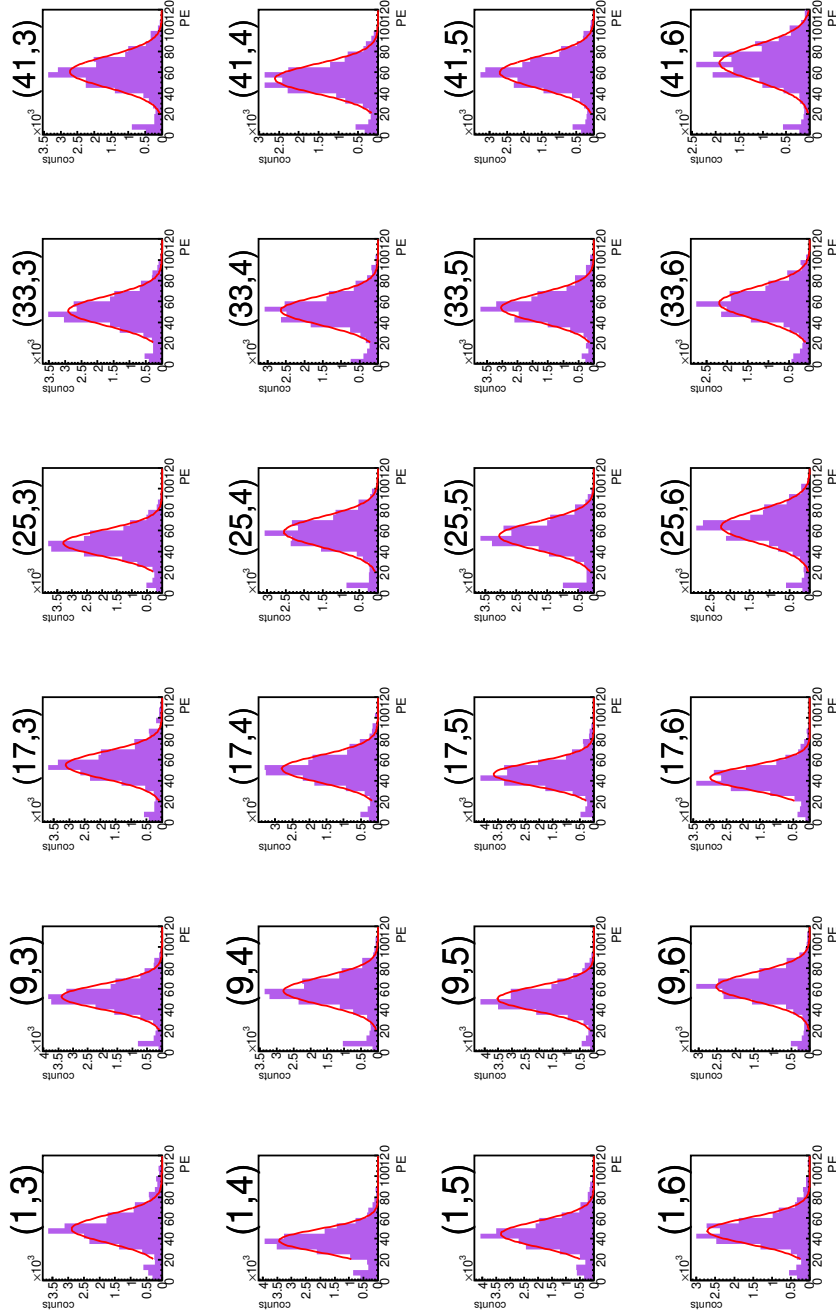
Figure 4.7: PE distribution per fiber in the (z,y) direction for MIPs.The red curve corresponds to the gaussian fitted for each fiber.
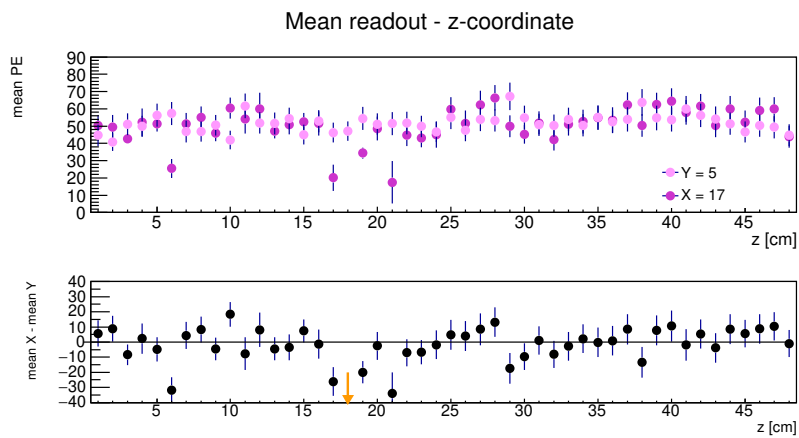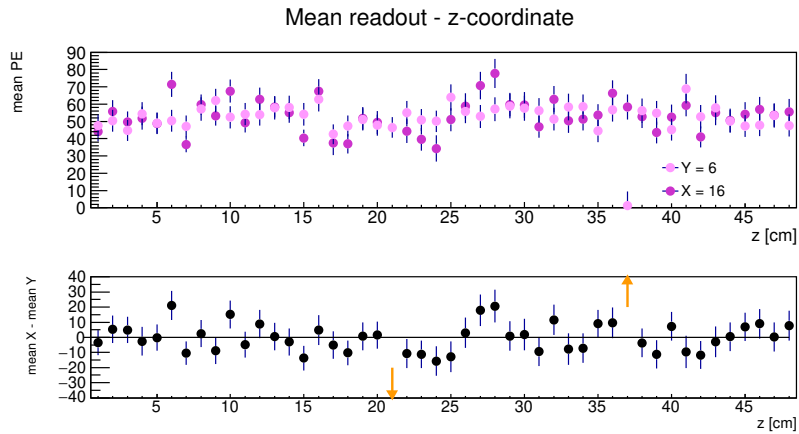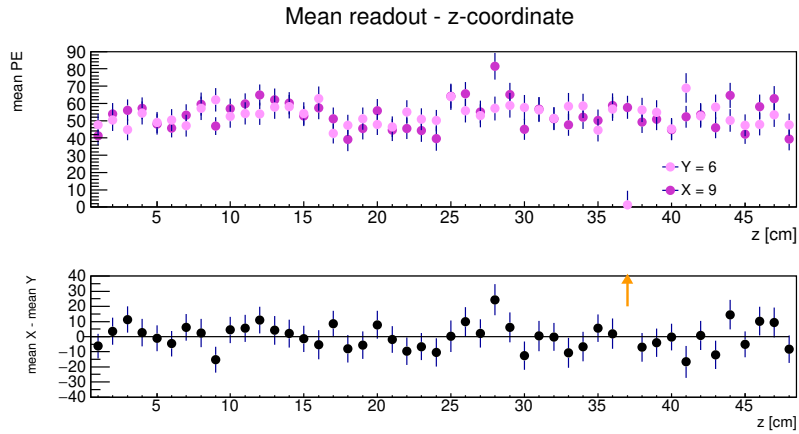
Figure 4.8: Example of x- and y- fibers readouts for different coordinates configurations.
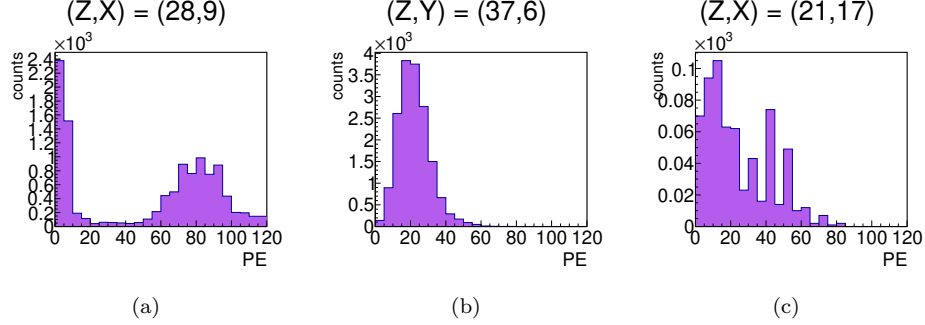
Figure 4.9: Examples of distributions whose fitted means significantly differ from the ~ 50 PE MIP peak.

consider Figure 4.10, where we show the mean readouts for all the horizontal and vertical transverse fibers, and in Figure 4.11, where the mean PE value for each fiber is shown for all those fibers where the fit converges and return positive mean values. There is an evident shift towards lower values for the vertical fibers with z-coordinate from 17 to 24, exactly corresponding to the Type-II MPPCs, whereas the mean is rather homogeneous in the other areas. There are some ~ 100 PE peaks and ~ 20 PE minima for the vertical x-fibers, that are probably due to low statistics and unability to properly resolve the peaks, as their concentration becomes drastically lower when we get closer to the detector axis $x = 12$, where the mean PE distribution becomes more homogeneous. The horizontal y-fibers have a much lower spread of values, probably due to higher statistics, and the the defect in the $y = 6$ fiber that we saw before clearly emerges in the lower diagram of figure 4.11.

Another feature that appears from Figures 4.10 and 4.11 is that for the vertical fibers, from $z = 25$ to $z = 28$ the average readout is higher than in the rest of the detector (and specifically, the $z > 28$ fibers, connected to the same type of MPPCs). This is explained because the original MPPCs and cable bundles in this area were reported defective and replaced with spare ones, that might have a different voltage gain, and therefore not performing properly because of the potential set to the operating regime of the other ones.

As one final observation, we consider the distribution of the means for the peaks registered in each fiber shown in Figure 4.12. Here we show the means for the fits on fibers equipped with Type-I MPPCs, also distinguishing between horizontal and vertical fibers. We have considered only vertical fibers close to the axis of the detector $x \in [4, 18]$ to avoid including the peaks and minima we discussed above, and only with coordinate $z \geq 30$ to get rid of the Type-II MP-PCs effects. For the horizontal fibers, we considered all the fibers shown in figure 4.11, except the $(z, y) = (38, 6)$. The parameters for the three distributions are summarized in table 4.3.

This corresponds to a energy resolution of approximately $\Delta E/E \sim 11\%$,
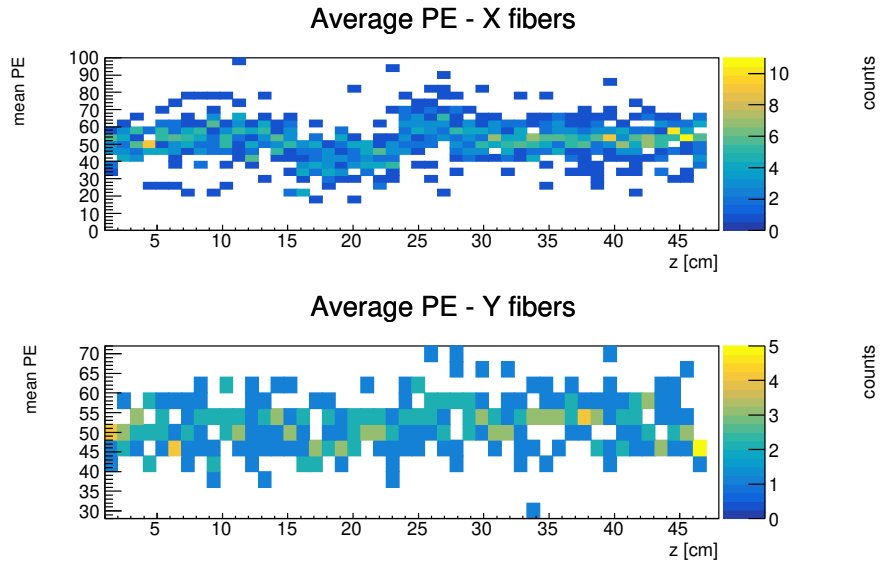
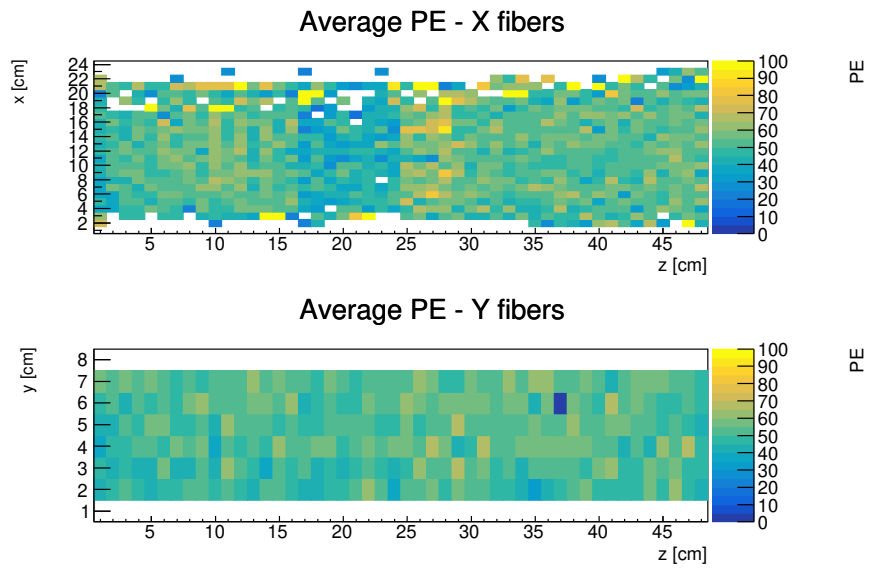Figure 4.10: Mean readout as function of the z-coordinate for all the horizontal-and vertical fibers.

Figure 4.11: Mean readout for each horizontal and vertical fiber.

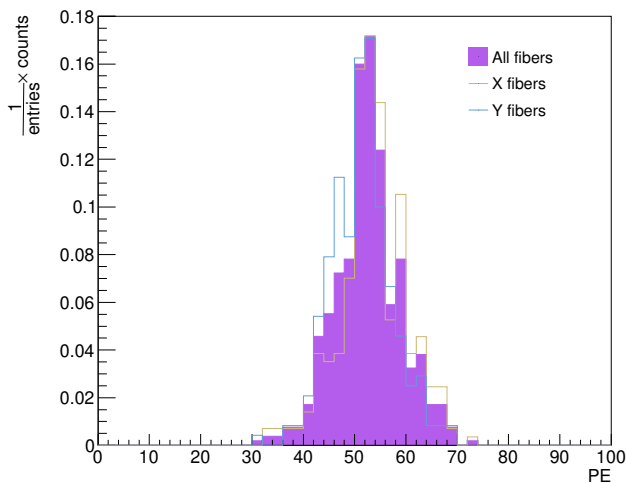Figure 4.12: MIP peaks distributions for all fibers, horizontal- only and vertical-only.

	mean [PE]	σ [PE]
All fibers	52.6	6.4
x - fibers	53.6	6.5
y - fibers	51.5	6.0

Table 4.3: Parameters extracted from the MIP peaks distributions in Figure 4.12.

which is indeed better than the $\sim 20\%$ MIP resolution indicated in the ND280 Technical design report before the upgrade [47].

The mean for the vertical x-fibers is slightly higher than the one for the horizontal ones. This might be due to the fact that we haven't excluded every defected MPPC, but also from the fact that the y-fibers are in total 16cm longer than the x-fibers, and net attenuation effects should be taken into account. According to the attenuation parameters in [7], we should in fact expect a $\sim 2PE$ difference between the median light yield from vertical and horizontal fibers.

4.4 Magnetic Field behaviour

An interesting effect to study is the way in which a magnetic field modifies the number of PEs measured in each fiber. As initial approach we should first estimate the minimum bending in the particle tracks, assuming that no energy is lost while traveling through the detector.

4.4.1 Minimum bending calculation.

As we know, a particle traveling through a magnetic field is subject to a force orthogonal to the direction of motion, called *Lorentz force*, with magnitude

$$F = q\,v\,B$$

where q is the charge of the particle, v its velocity and B the magnitude of the magnetic field.

This force causes a centripetal acceleration $a = \frac{v^2}{R}$, forcing the particle into a circular trajectory with radius R. Note that, since the force is orthogonal to the motion, there is no energy loss due to it. The Newton equation for the particle is then

$$m\frac{v^2}{R} = q\,v\,B,$$

from which we can extract the expression for the curvature radius

$$R = \frac{mv}{qB}. \tag{4.1}$$

At this point, we should express the velocity v in terms of the relativistic momentum

$$p = \gamma mv \qquad \text{with} \qquad \gamma := \left(1 - \frac{v^2}{c^2}\right)^{-\frac{1}{2}}$$

where $c = 3 \times 10^8\,\mathrm{m\,s^{-1}}$ is the speed of light in vacuum. Inverting this definition leads to the desired expression for the velocity of the particle

$$v(p) = p\left(m^2 + \frac{p^2}{c^2}\right)^{-\frac{1}{2}}. \tag{4.2}$$

If we plug equation 4.2 into 4.1 we can eventually express the curvature radius in terms of the particle momentum

$$R = \frac{p}{qB}\left(1 + \frac{p^2}{m^2c^2}\right)^{-\frac{1}{2}}. \tag{4.3}$$
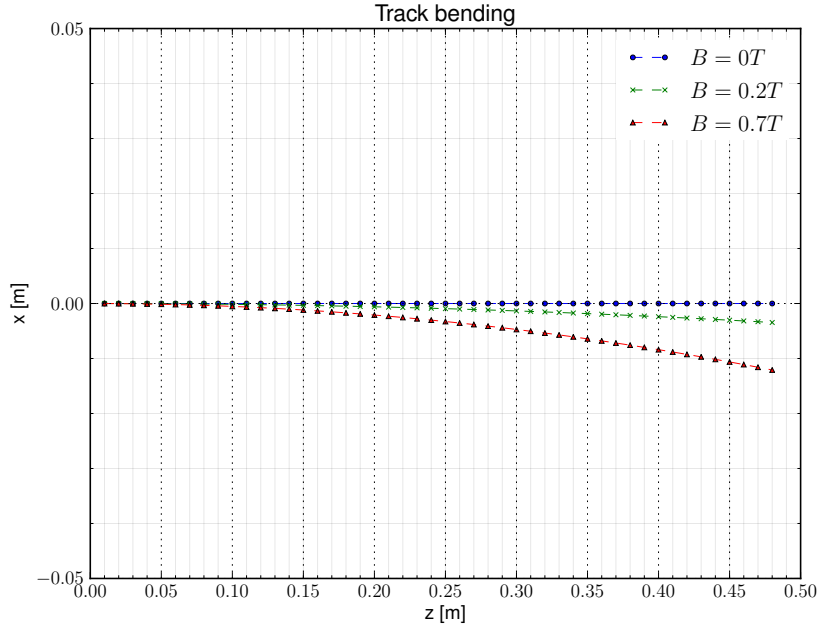
Figure 4.13: Analytical simulation of bending due to a magnetic field for a 2GeV/c muon. the grid lines correspond to the cubes edges.

The trajectory of a particle in the (z, x) plane with entry point the origin can then be obtained by inserting expression 4.3 in the circumference equation $x^2 + (y - R)^2 = R^2$ and choosing one of the two solutions $y = y(x)$:

$$y = \sqrt{R^2 - x^2} - R.$$

Figure 4.13 shows this trajectory for a 2GeV/c muon ($m = 0.106\text{GeV}/c^2$, $q = -e$) [63] for the three different values of magnetic field in the dataset. The units of the grid correspond to the edges of each cube, to have an idea of the trajectories inside the detector.

We can see that we have a noticeable $\sim 2.5\%$ deviation at the end from the zero-field trajectory (B=0T) only for the strongest magnetic field $B = 0.7$T, whereas for $B = 0.2$T the trajectory remains confined within the same cubes for the whole detector length.

4.4.2 Search for bending effects on the dataset

When we consider the data, we first want to discriminate between straight (magnet off) and bent (magnet off) tracks. The first issue we encounter is the

	n. events	% of raw data set
magnet off	4073	$\sim 17\%$
magnet on	1235748	$\sim 81\%$

Table 4.4: Size of magnet-on (0.2T and 0.7T) and magnet-off muons dataset.

lack of statistics for magnet off events with the MIP cuts we have introduced in section 4.3 (returning 444 events). We then decide to remove those selection criteria and keep only the time-from-trigger requirement in order to keep a maximum number of events. Table 4.4 provides some information on the events we consider in this section. We immediately note that the dataset without bending field is much smaller than the one for the runs when the magnet was on.

In order to try to compare the two datasets, we consider the distribution of the MIP peaks for each vertical and horizontal fiber with the same z-coordinate and take its mean value. We consider only those peaks fitted with a gaussian (in the same range as for the MIP analysis) with mean value at least 10PE in order to be sure we haven't included also the zero-peaks. To be sure that the fit converges and actually corresponds to a MIP peak we only consider the entries for which the standard deviation is less than 30PE. In Figure 4.14 we show those distributions for horizontal and vertical fibers.

We see that these measurements are dominated by statistical noise and it is impossible to discriminate any underlying pattern that hints incompatibility between the averages for the two different magnetic field settings.

In order to try to get rid of some statistical noise and obtain a clearer signal we consider only the *magnet on* data, and we discriminate between $B = 0.2$T and $B = 0.7$T for 2GeV/c muons. Table 4.5 summarizes the magnitude of these two datasets once we have reintegrated the MIP selection due to the higher number of events.

	n. events	% of raw data set
MIP - 0.2T	71172	$\sim 8\%$
MIP - 0.7T	38860	$\sim 7\%$

Table 4.5: Size of B=0.2Tn and B=0.2T muons dataset.

In Figure 4.15 we show the same distribution for the horizontal fibers, where we have more statistics and therefore it can be more instructive to consider. Here, even though the measurement is still dominated by uncertainty, we can however note that the difference between the two fields is more stable. It looks like there might be some systematic noise that leads the 0.7T peaks to be at slightly less PEs than the 0.2T ones, even though we would expect them to match for lower z-coordinates. Here the deviation of the tracks from the beam
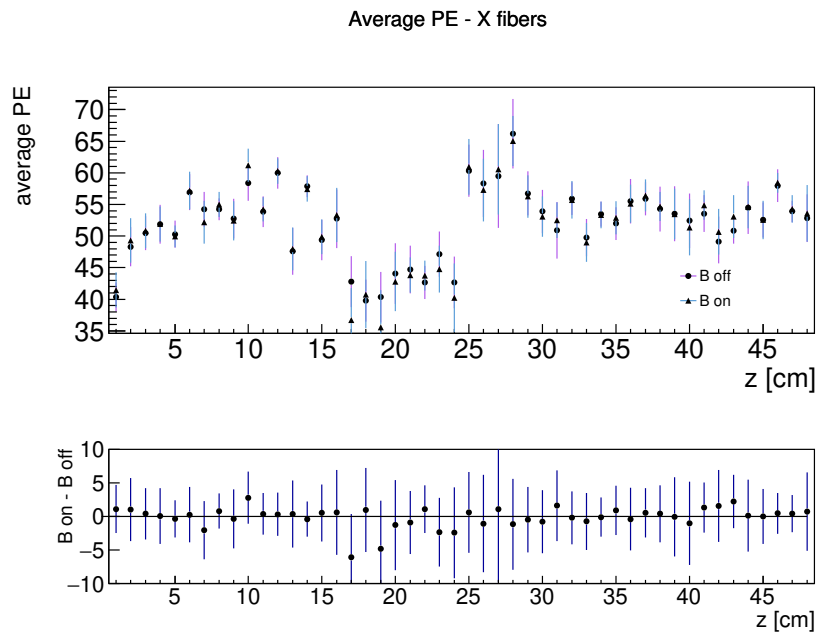
(a)
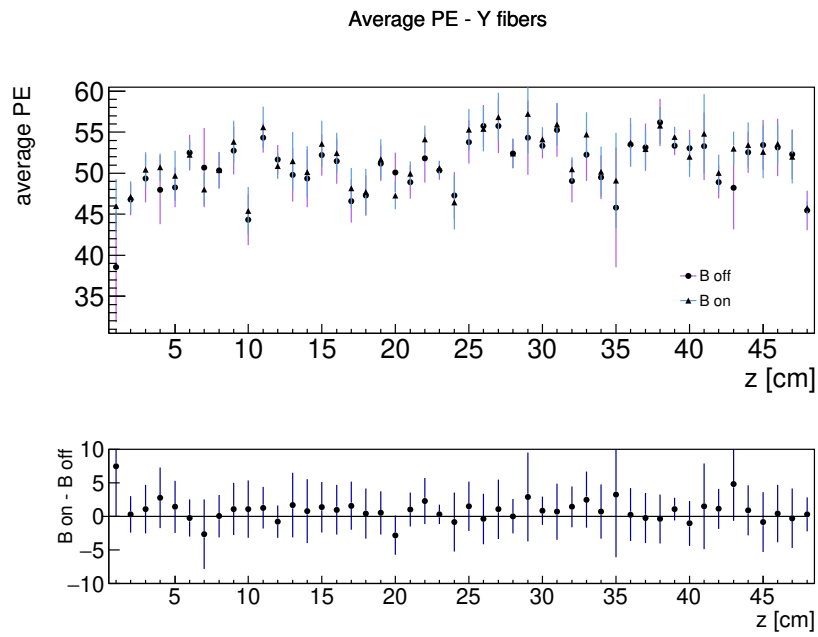
(b)

Figure 4.14: Average PE peak for a MIP, for (a) vertical and (b) horizontal fibers.
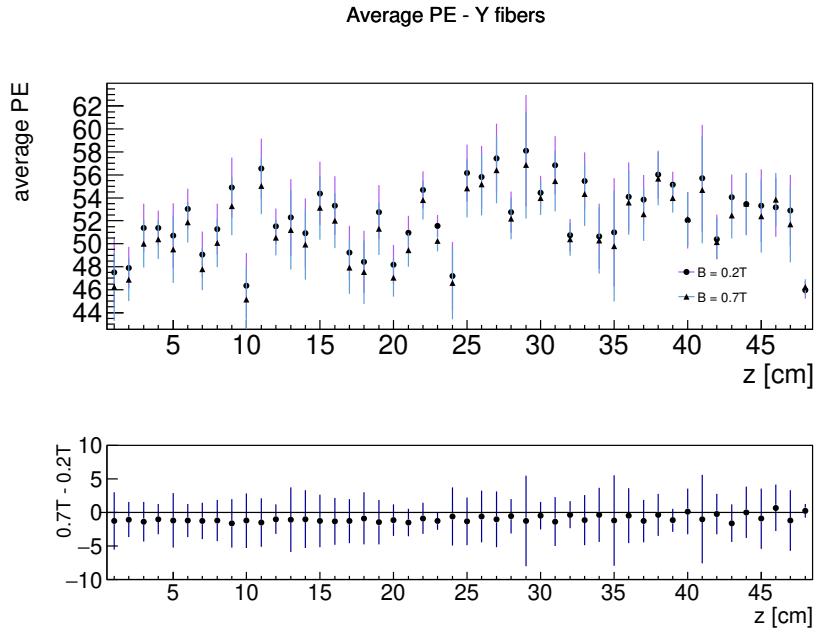
Figure 4.15: Average MIP PE peak in the horizontal fibers for each Z coordinate and different magnetic field settings: B=0.2T and B=0.7T.

axis is in fact irrelevant and thus there should be no difference in energy loss while traveling across the cubes, as the distance travelled inside the cube is the same and coincides approximately with the cube side for straight tracks. If we assume the presence of this systematic uncertainty, whose origin is not well understood, as a shift in the 0.7T average peaks, we see that the PE yield for the 0.7T slightly increases towards higher z. This should be expected as here the bending starts to be noticeable as the distance traveled inside each cube tends more towards the diagonal of the cube itself.

Finally, if we try to plot the peak distributions for $z > 32$, as we show in Figure 4.16, we can notice that indeed, the distribution for $B = 0.7$T looks indeed slightly shifted towards higher PEs. The averages and standard deviations for those distributions are summarized in Table 4.6

The values are at all effects compatible with each other and, since they differ for less than one count, to be able to make stronger claims we would need to improve the statistics, and thus the resolution of our measurement. The August-September run focuses in fact on the behaviour of different particles in a 0.2T magnetic field, that will be the one used in T2K. It could be interesting to consider also the June-July 2018 run, that contains a large number of those

events we want to select in this analysis.

Average PE readout
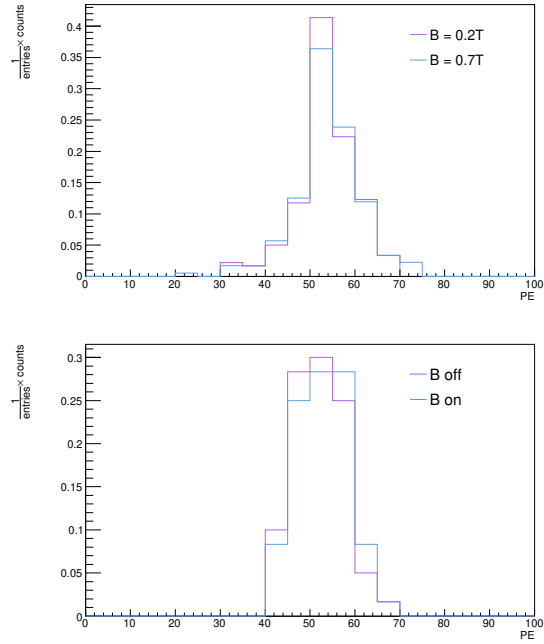
Figure 4.16: Peak distributions for 2GeV/c MIPs read at the end of detector - $z \geq 32$.

X - fibers		
B [T]	mean [PE]	σ [PE]
0.2	53.3	6.5
0.7	53.9	7.1
Y - fibers		
B [T]	mean [PE]	σ [PE]
0.2	52.4	5.6
0.7	52.9	5.6

Table 4.6: Average MIP peak distributions for $z > 32$ for the different magnetic fields B=0.2T and B=0.7T.

Chapter 5

Discussions and conclusions

Beam test data The study on the Minimum Ionizing Particle (MIP) response has allowed us to show the features of the electronics and WLS fibers, and identify eventual malfunctions due to defective devices. The average MIP light yield of 52.6 ± 6.4 p.e. (photoelectrons) is in good agreement with tests on other geometries for the SuperFGD cubes. For instance, the test of a 3×3 array equipped with Type II MPPCs with cosmic muons provides a mean yield of ~ 55 photoelectrons (including higher energy tails)[15]. The corresponding $\sim 11\%$ $\Delta E/E$ resolution improves the previous ND280 FGD $\sim 20\%$ resolution before the upgrade [47]. The improved energy resolution adds up to the good tracking resolution provided by the cubes array concept, thus reducing the overall systematic uncertainties for future experiments.

The tentative search for magnetic bending effects did not lead to clear results, as we did not manage to resolve any significant light yield variation between different field intensities. This however should not be too surprising, as the effect reported in [63, 13] refers essentially to the behaviour of electrons, which loose a significant amount of energy while traveling across a medium and thus the bending effect becomes more significant. It could be interesting to consider such effect for different particle species, developing and optimizing some basic Particle Identification algorithms, and for a larger $B = 0$T statistics, in order to have a more precise *field off* reference, that would significantly reduce the noise and make the comparison with different bending trajectories more clear and efficient.

SuperFGD as concept for future neutrino experiments The SuperFGD design proves to be effective in terms of energy resolution. Its peculiar geometry as a 3D voxel array allows in addition a good precision in track reconstruction, being able to discriminate easily between different events and provide some easy preliminary tags. The good tracking possibilities make it a great candidate for future neutrino experiments where high precision is required, providing enough information for precise reconstruction of the interaction vertices. It is also an extremely versatile device because of the simplicity when it comes to increasing

the active detector area -we just require some extra cube layers and longer WLS fibers. This allows us to adapt the geometry for different experiment designs, depending on the features of the beams used. Increasing the active volume grants good resolution for low energy neutrino scattering events, where the angular distribution is less defined and more isotropic, as is the case for the ESSνSB design. Despite some further work is needed to have a clear understanding of the detector behaviour, for instance in terms of the low-energy peaks suppression, the versatility of SuperFGD makes it a great candidate detection device for many new experiments, and it is thus destined to play a significant role in detection techniques in the next generation of experiments, possibly also outside of the neutrino physics field.

Overview and outlook Throughout this thesis we have provided an overview of the current results and future development in neutrino research, with a particular focus on CP violation precision measurements that can give further insight on the matter-antimatter asymmetry problem. We have focused on the novelty and outreach potential from the construction of a neutrino beam line at the European Spallation Source in Sweden, which would rely on upgrading the plan for a LINAC that is already being constructed and would potentially become a benchmark for the European research community, providing the world's most intense neutrino source. The novelty of the ESS neutrino Super Beam (ESSνSB) resides in the fact that it is tuned to measure neutrino oscillations at the second oscillation peak, motivated by the fact that for a relatively large $\theta_{13} \sim 8°$ mixing angle this peak is more sensitive to matter-antimatter interference effects with respect to measurements taken on the first oscillation peak, like the ones that will come from T2HK and DUNE. In this context, the SuperFGD design finds broad usage due to its versatility and good time and energy resolution.

The focus on improving the resolution and reducing systematic uncertainties in neutrino oscillation measurements will eventually allow us to get new fundamental insights in neutrino physics. Promising results on determining the value of the CP phase δ have recently come from T2K, and a further upgrade in the detection techniques could allow to reach the necessary discovery significance. This will also allow us to get closer to the solution of the neutrino hierarchy problem and the determination of neutrino masses, as well as provide new constraints on the Majorana neutrino models. The latter research direction will proceed parallel to collider experiments searching for Majorana mass terms contributions to cross sections and new physics in general.

Bibliography

[1] R. et al. Aaij. "Measurement of CP asymmetry in D0→KK+ decays". In: *Physics Letters B* 767 (Feb. 2017).

[2] K. et al. Abe. "Observation of Large *CP* Violation in the Neutral *B* Meson System". In: *Phys. Rev. Lett.* 87 (9 Aug. 2001), p. 091802.

[3] K. et al. Abe. "The T2K experiment". In: *Nuclear Instruments and Methods in Physics Research Section A: Accelerators, Spectrometers, Detectors and Associated Equipment* 659.1 (Dec. 2011), pp. 106–135.

[4] E. et al. Abouzaid. "Precise measurements of direct *CP* violation, *CPT* symmetry, and other parameters in the neutral kaon system". In: *Phys. Rev. D* 83 (9 May 2011), p. 092001.

[5] Q. R. et al. Ahmad. "Direct Evidence for Neutrino Flavor Transformation from Neutral-Current Interactions in the Sudbury Neutrino Observatory". In: *Phys. Rev. Lett.* 89 (1 June 2002), p. 011301.

[6] M. et al. Aker. "Improved Upper Limit on the Neutrino Mass from a Direct Kinematic Method by KATRIN". In: *Phys. Rev. Lett.* 123 (22 Nov. 2019).

[7] A. Blondel et al. *The SuperFGD Prototype Charged Particle Beam Tests.* 2020. arXiv: 2008.08861 [physics.ins-det].

[8] Barkas et al. "Mass-Ratio Method Applied to the Measurement of L-Meson Masses and the Energy Balance in Pion Decay". In: *Phys. Rev.* 101 (2 1956).

[9] K. Abe et al. *T2K ND280 Upgrade - Technical Design Report.* 2019. eprint: arXiv:1901.03750.

[10] B. et al. Aubert. "Measurement of *CP*-Violating Asymmetries in B^0 Decays to *CP* Eigenstates". In: *Phys. Rev. Lett.* 86 (12 Mar. 2001), pp. 2515–2522.

[11] Louis J. Basile. "Transfer of excitation energy in rigid solutions of organic scintillators". In: *Trans. Faraday Soc.* 60 (0 1964), pp. 1702–1714.

[12] A. de Bellefon et al. *MEMPHYS:A large scale water Cerenkov detector at Fréjus.* 2006. arXiv: hep-ex/0607026 [hep-ex].

[13] M. Bertoldi et al. "Scintillators in magnetic fields up to 20-T". In: *Nucl. In-strum. Meth. A* 386 (1997), pp. 301–306. DOI: 10.1016/S0168-9002(96)01178-3.

[14] J B Birks. In: *Proceedings of the Physical Society. Section A* 64.10 (Oct. 1951), pp. 874–877.

[15] A. Blondel et al. "A fully-active fine-grained detector with three readout views". In: *Journal of Instrumentation* 13.02 (Feb. 2018), P02006–P02006. ISSN: 1748-0221. DOI: 10.1088/1748-0221/13/02/p02006. URL: http://dx.doi.org/10.1088/1748-0221/13/02/P02006.

[16] A Blondel, M Yokoyama, and M Zito. *The T2K-ND280 upgrade pro-posal*. Tech. rep. CERN-SPSC-2018-001. SPSC-P-357. This proposal is the follow-up of the Expression of Interest EOI-15 submitted to SPSC in January 2017. Geneva: CERN, Jan. 2018.

[17] S. Boyd. *Neutrino Mass and direct measurements*. Mar. 2014.

[18] R. Brun and F. Rademakers. "ROOT: An object oriented data analysis framework". In: *Nucl. Instrum. Meth. A* 389 (1997). Ed. by M. Werlen and D. Perret-Gallix, pp. 81–86.

[19] Nicola Cabibbo. "Unitary Symmetry and Leptonic Decays". In: *Phys. Rev. Lett.* 10 (1963), pp. 531–533.

[20] L. Cardani. "Neutrinoless Double Beta Decay Overview". In: (2018). arXiv: 1810.12828 [nucl-ex].

[21] J.H. Christenson et al. "Evidence for the 2π Decay of the K_2^0 Meson". In: *Phys. Rev. Lett.* 13 (1964), pp. 138–140.

[22] DUNE collaboration. *Deep Underground Neutrino Experiment*. URL: https://www.dunescience.org/.

[23] T2K Collaboration. "Constraint on the matter–antimatter symmetry-violating phase in neutrino oscillations". In: *Nature* 580 (July 2020).

[24] Pilar Coloma and Enrique Fernandez-Martinez. "Optimization of neutrino oscillation facilities for large 13". In: *Journal of High Energy Physics* 2012 (Oct. 2011). DOI: 10.1007/JHEP04(2012)089.

[25] Pilar Coloma et al. "Systematic uncertainties in long-baseline neutrino oscillations for large13". In: *Physical Review D* 87.3 (Feb. 2013). ISSN: 1550-2368. DOI: 10.1103/physrevd.87.033004. URL: http://dx.doi.org/10.1103/PhysRevD.87.033004.

[26] Landau L. D. "On the energy loss of fast particles by ionization". In: *The Collected papers of L. D. Landau* 56 (1965), p. 417.

[27] CERN Engineering Department. *East Area Documentation*. URL: http://sba.web.cern.ch/sba/BeamsAndAreas/East/East.htm.

[28] Tord Ekelof and Marcos Dracos. "The design and performance of the ESS Neutrino Super Beam project ESSνSB". In: *PoS* NOW2018 (2019). Ed. by Antonio Marrone, Alessandro Mirizzi, and Daniele Montanino, p. 029. DOI: 10.22323/1.337.0029. arXiv: 1903.08437 [physics.ins-det].

[29] F. Englert and R. Brout. "Broken Symmetry and the Mass of Gauge Vector Mesons". In: *Phys. Rev. Lett.* 13 (9 Aug. 1964), pp. 321–323.

[30] J. A. Formaggio and G. P. Zeller. "From eV to EeV: Neutrino cross sections across energy scales". In: *Rev. Mod. Phys.* 84 (3 Sept. 2012), pp. 1307–1341. DOI: `10.1103/RevModPhys.84.1307`. URL: `https://link.aps.org/doi/10.1103/RevModPhys.84.1307`.

[31] S. Fukuda et al. "Solar B-8 and hep neutrino measurements from 1258 days of Super-Kamiokande data". In: *Phys. Rev. Lett.* 86 (2001), pp. 5651–5655. DOI: `10.1103/PhysRevLett.86.5651`. arXiv: `hep-ex/0103032`.

[32] Y. et al. Fukuda. "Evidence for Oscillation of Atmospheric Neutrinos". In: *Phys. Rev. Lett.* 81 (8 Aug. 1998), pp. 1562–1567.

[33] Y. Fukuda et al. "Evidence for oscillation of atmospheric neutrinos". In: *Phys. Rev. Lett.* 81 (1998), pp. 1562–1567.

[34] Howard Georgi and S. L. Glashow. "Unity of All Elementary-Particle Forces". In: *Phys. Rev. Lett.* 32 (8 Feb. 1974), pp. 438–441.

[35] Sheldon L. Glashow. "The renormalizability of vector meson interactions". In: *Nucl. Phys.* 10 (1959), pp. 107–117.

[36] M. Gonzalez-Garcia et al. "Global fit to three neutrino mixing: Critical look at present precision". In: *Journal of High Energy Physics* 2012 (Sept. 2012).

[37] Eirik Gramstad. "Neutrino CP Violation with the European Spallation Source neutrino Super Beam project". In: *Journal of Physics: Conference Series* 1468 (Feb. 2020), p. 012119. DOI: `10.1088/1742-6596/1468/1/012119`. URL: `https://doi.org/10.1088%2F1742-6596%2F1468%2F1%2F012119`.

[38] David J Griffiths. *Introduction to electrodynamics; 4th ed.* Re-published by Cambridge University Press in 2017. Boston, MA: Pearson, 2013.

[39] Peter W. Higgs. "Broken Symmetries and the Masses of Gauge Bosons". In: *Phys. Rev. Lett.* 13 (16 Oct. 1964), pp. 508–509.

[40] C. Jarlskog. "A Basis Independent Formulation of the Connection Between Quark Mass Matrices, CP Violation and Experiment". In: *Z. Phys. C* 29 (1985), pp. 491–497.

[41] William R Leo. *Techniques for nuclear and particle physics experiments: a how-to approach.* Berlin: Springer, 1994.

[42] B. D. Leverington. *An overview of scintillators and their application in High Energy Physics.* Heidelberg - HighRR Seminar. 2017. URL: `https://indico.cern.ch/event/602044/contributions/2429699/attachments/1426301/2188333/scintillatorseminar.pdf`.

[43] J. Lindhard. "On the properties of a gas of charged particles". In: *Dan. Mat.-Fys. Medd.* 28 (8 1954).

[44]   J Lopez-Pavon. *Leptogenesis and CP violation in the leptonic sector.* ESSνB annual meeting talk. 2017. URL: `https://indico.in2p3.fr/event/17355/contributions/66491/attachments/50892/65149/Leptogenesis_CP.pdf`.

[45]   J.S. Coursey M.J. Berger and M.A. Zucker. *ESTAR, PSTAR, and AS-TAR: Computer Programs for Calculating Stopping-Power and Range Tables for Electrons, Protons, and Helium Ions.* Tech. rep. Gaithersburg, MD: NIST, 2017.

[46]   Ziro Maki, Masami Nakagawa, and Shoichi Sakata. "Remarks on the unified model of elementary particles". In: *Prog. Theor. Phys.* 28 (1962), pp. 870–880.

[47]   *ND280 Technical Design Report (2006).* URL: `http://www.nd280.org/convenors/ND280%5C%20Review%5C%20document%5C%202006/tdr.pdf/view`.

[48]   Etam Noah et al. "Readout scheme for the Baby-MIND detector". In: *PoS* PhotoDet2015 (2016), p. 031.

[49]   W. Pauli. "On the Connection between Spin and Statistics". In: *Progress of Theoretical Physics* 5.4 (July 1950), pp. 526–543.

[50]   W. Pauli. "The Connection Between Spin and Statistics". In: *Phys. Rev.* 58 (8 Oct. 1940), pp. 716–722.

[51]   John A Peacock. *Cosmological physics; rev. version.* Cambridge: Cambridge Univ., 1999.

[52]   Michael E. Peskin and Daniel V. Schroeder. *An Introduction to quantum field theory.* Reading, USA: Addison-Wesley, 1995. ISBN: 978-0-201-50397-5.

[53]   Planck Collaboration. "Planck 2013 results. XVI. Cosmological parameters". In: *A&A* 571 (2014), A16.

[54]   B. Pontecorvo. "Neutrino Experiments and the Problem of Conservation of Leptonic Charge". In: *Sov. Phys. JETP* 26 (1968), pp. 984–988.

[55]   ESS Neutrino Super Beam Design Study Project. URL: `https://euronunet.in2p3.fr/about-us/`.

[56]   EuroNuNet networking project. URL: `https://euronunet.in2p3.fr/about-us/`.

[57]   X. Qian and P. Vogel. "Neutrino Mass Hierarchy". In: *Prog. Part. Nucl. Phys.* 83 (2015), pp. 1–30. arXiv: `1505.01891 [hep-ex]`.

[58]   Press Release he Royal Swedish Academy of Sciences. *The Nobel Prize in Physics 2015.* Oct. 2015. URL: `https://www.nobelprize.org/uploads/2018/06/press-30.pdf`.

[59]   A.D. Sakharov. "Violation of CP Invariance, C asymmetry, and baryon asymmetry of the universe". In: *Sov. Phys. Usp.* 34.5 (1991), pp. 392–393. DOI: `10.1070/PU1991v034n05ABEH002497`.

[60]   Jun John Sakurai. *Modern quantum mechanics; rev. ed.* Reading, MA: Addison-Wesley, 1994.

[61]   Abdus Salam and John Clive Ward. "Electromagnetic and weak interactions". In: *Phys. Lett.* 13 (1964), pp. 168–171.

[62]   R. M. Sternheimer. "The Density Effect for the Ionization Loss in Various Materials". In: *Phys. Rev.* 88 (4 1952), pp. 851–859.

[63]   Tanabashi et al. "Review of Particle Physics". In: *Phys. Rev. D* 98 (3 2018).

[64]   Mark Thomson. *Modern particle physics.* New York: Cambridge University Press, 2013.

[65]   E A Uehling. "Penetration of Heavy Charged Particles in Matter". In: *Annual Review of Nuclear Science* 4.1 (1954), pp. 315–350.

[66]   P.V. Vavilov. "Ionization losses of high-energy heavy particles". In: *Sov. Phys. JETP* 5 (1957), pp. 749–751.

[67]   Steven Weinberg. "A Model of Leptons". In: *Phys. Rev. Lett.* 19 (21 Nov. 1967), pp. 1264–1266.

[68]   Lincoln Wolfenstein. "Parametrization of the Kobayashi-Maskawa Matrix". In: *Phys. Rev. Lett.* 51 (1983), p. 1945.

[69]   A. Zee. *Quantum field theory in a nutshell.* Nov. 2003. ISBN: 978-0-691-14034-6.